Studies of anisotropy of iron based superconductors

by

Jason A. Murphy

A thesis submitted to the graduate faculty

in partial fulfillment of the requirements for the degree of

MASTER OF SCIENCE

Major: Condensed Matter Physics

Program of Study Committee:

Ruslan Prozorov, Major Professor

Makariy A. Tanatar

Charles Kerton

Kevin deLaplante

Iowa State University

Ames, Iowa

2013

DEDICATION

I would like to dedicate this thesis to my family and friends that have helped me so much through out, my graduate and undergraduate school years. In particular I would like to thank my parents Rhonda Murphy and Steve Murphy.

TABLE OF CONTENTS

LIST OF FIGURES

ACKNOWLEDGEMENTS

To everyone that has helped in my time spent at Iowa State University, I would like to say, thank you. In particular I would like to thank my major professor Dr. Ruslan Prozorov. To Dr. Makariy Tanatar thank you for all of the questions you made me answer until I figured out or found the answer. Thank you to Dr. Charles Kerton for giving me my first physics job nearly 9 years ago and for agreeing to be on my comity.

To the rest of the members of the Prozorov Lab, Thank you for all your help and friendship in and out of the lab.

Having spent 9 years in the Iowa State Physics and Astronomy department, I can't thank everyone that I would like to. However, I would like thank Bert Crawley for all the help with the Physics and Astronomy Club and any other strange project I could come up with, and Jim Cochran for all the conversations and help over the year.

To Melissa Linde, Thank you for all the love and support.

ABSTRACT

To study the electronic anisotropy in iron based superconductors, the temperature dependent London penetration depth, $\Delta\lambda(T)$, have been measured in several compounds, along with the angular dependent upper critical field, $H_{c2}(T)$. Study was undertaken on single crystals of $Ba(Fe_{1-x}Co_x)_2As_2$ with x=0.108 and x=0.127, in the overdoped range of the doping phase diagram, characterized by notable modulation of the superconducting gap. Heavy ion irradiation with matching field doses of 6 T and 6.5 T respectively, were used to create columnar defects and to study their effect on the temperature $\Delta\lambda(T)$. The variation of the low-temperature penetration depth in both pristine and irradiated samples was fitted with a power-law function $\Delta\lambda(T) = AT^n$. Irradiation increases the magnitude of the pre-factor A and decreases the exponent n, similar to the effect on the optimally doped samples. This finding supports the universal $s_{\pm}$ scenario for the whole doping range. Knowing that the $s_{\pm}$ gap symmetry exists across the superconducting dome for the electron doped systems, we next looked at $\lambda(T)$, in optimally - doped, $SrFe_2(As_{1-x}P_x)_2$, x =0.35. Both, as-grown ($T_c \approx$25 K) and annealed ($T_c \approx$35 K) single crystals of $SrFe_2(As_{1-x}P_x)_2$ were measured. Annealing decreases the absolute value of the London penetration depth from $\lambda(0) = 300 \pm 10$ nm in as-grown samples to $\lambda(0) = 275 \pm 10$ nm. At low temperatures, $\lambda(T) \sim T$ indicates a superconducting gap with line nodes. Analysis of the full-temperature range superfluid density is consistent with the line nodes, but differs from the simple single-gap $d-$wave. The observed behavior is very similar to that of $BaFe_2(As_{1-x}P_x)_2$, showing that isovalently substituted pnictides are inherently different from the charge-doped materials. In-plane resistivity measurements as a function of temperature, magnetic field, and its orientation with respect to the crystallographic ab-plane were used to study the upper critical field, H_{c2}, of two overdoped compositions of $Ba(Fe_{1-x}Ni_x)_2As_2$,

x=0.054 and x=0.072. Measurements were performed using precise alignment (with accuracy less than 0.1^o) of the magnetic field with respect to the Fe-As plane. The dependence of the H_{c2} on angle θ between the field and the *ab*-plane was measured in isothermal conditions in a broad temperature range. We found that the shape of the H_{c2} vs. θ curve clearly deviates from the Ginzburg-Landau theory.

CHAPTER 1.   Introduction

One of the most interesting and possibly technically useful phenomenon in condensed matter physics is that of superconductivity. It was discovered by H. K. Onnes in 1911 when he observed that the electrical resistance of Mercury dropped to zero when cooled to 4.2 K. Superconductivity is observed as a sudden drop of resistance to zero when material is cooled below a critical temperature known as T_c. Because this is one of the main parameters of a superconductor, the search for materials with higher transition temperates is one of the main lines of research in materials and condensed matter physics. An important discovery in superconducting science was made in 2008 when $LaFeAO_{1-x}$ was found to superconduct below $T_c \sim 26\ K$ [Kamihara et al. [2008]]. This discovery opened up the world of high temperature iron based superconductors or iron pnictides. Five of the most heavily studied groups of compounds are, FeSe known as "11", AFeAs (A refers to Alkaline metals) known as "111", RFeAsO (R refers to Rare Earth) known as "111", $AEFe_2Pn_2$ (again AE is Alkaline Earth and Pn refers to a Pnictogen) known as "122", and finally $Sr_3Sc_2O_5Fe_2As_2$. This work is entirely concerned with the 122 Fe based superconductors, more specifically $Ba(Fe_{1-x}Co_x)_2As_2$, $Ba(Fe_{1-x}Ni_x)_2As_2$, and $SrFe_2(As_{1-x}P_x)_2$)(see figure 1.1) [Canfield and Bud'ko [2010],Johnston [2010],Paglione and Greene [2010]].

It took nearly 50 years after the initial discovery of superconductivity for a microscopic theory to come about, published by John Bardeen, Leon Neil Cooper, and John Robert Schriefer (BCS theory) [J. Bardeen [1957]] in 1957. In some ways its successes can not be over stated even to the point of being given the Nobel Prize in 1972.
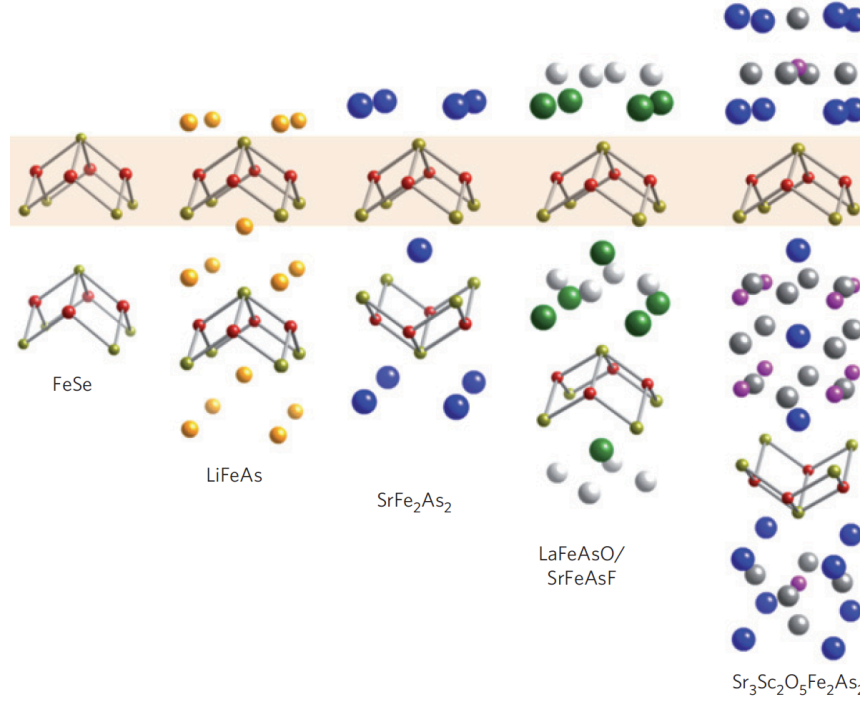
Figure 1.1 Crystal structure of iron based superconductors with Fe-As units highlighted. FeSe "11", LiFeAs "111", $SrFe_2Pn_2$ "122", LiFeAsO "1111", and finally $Sr_3Sc_2O_5Fe_2As_2$ [Paglione and Greene [2010]]

The superconductors described by BCS theory became known as BCS superconductors. In the simplest case BCS superconductors have a single superconducting energy gap that forms at the Fermi level, when cooled below a critical transition temperature. In BSC theory the electrons form bound pairs on cooling below the transition temperature. These bound electron pairs became known as Cooper pairs. The pairing mechanism which overcomes the Coulomb repulsion for these systems is an electron-phonon interaction. The magnitude of the energy gap is directly related to the superconducting transition temperature T_c. While the T_c varies widely across superconducting systems, BCS theory sets an approximate upper limit of $T_c \sim 30$ K. Similar to sufficiently high temperature being able to destroy superconductivity, a large enough magnetic field can not only reduce the transition temperature but also destroy superconductivity. This field is known as the critical field H_c. There are two types of superconductors. Type *I*

superconductors are characterized by a single critical field H_c. Type *II* superconductors have a lower critical field H_{c1}, above H_{c1} field penetrates the sample in the form of vortices, each vortex containing a single flux quantum[Abrikosov [1957]]. As the field increases, it becomes more energetically favorable to form more vortices, due to negative surface energy at the superconducting and normal interface, it is favorable to create the largest possible interface. As there are more and more vortices, the whole of the superconducting volume is taken up by the normal cores of neighboring vortices and at some field known as the second critical field, H_{c2}, superconductivity is fully suppressed. Even in the case of an extremely small magnetic field, there will be some penetration into the bulk of the sample. The field screening occurs at some distance known as the London penetration depth [London [1950]] which is a characteristic distance in both type *I* and type *II* systems.

The understanding of full-gap, s-wave, superconductors (see fig 1.2) seemed to be complete, when IBM physicists M*ü*ller and Bednorz discovered superconductivity in $La_{2-x}Ba_xCuO_4$ with a T_c=35 K [M*ü*ller and Bednorz [1987]]. Within a year the maximum T_c for this new class of superconductor had risen to $T_c \sim 93\ K$ Y-Ba-Cu-O. This limit has been pushed even further in the past 26 years up to 156 K in the mercury based material under pressure. Not only does this new class have T_c significantly higher than conventional BCS estimations, they turned out to be of a very different kind.

As was stated earlier, s-wave superconductors have a spherical symmetric energy gap that governs their properties. It turned out that the new class of superconductors, cuprates, do not have the same type of an energy gap. These system became known as d-wave superconductors due to the x-y plane lobed symmetry of there gap (see fig1.2) [Tsuei and Kirtley [2000]]. To many researchers this difference in gap symmetry along with the other differences in properties implied that the mechanism generating the pairing of electrons into Cooper pairs was not the same as in BCS superconductors. It has been shown that a magnetic spin interaction may be
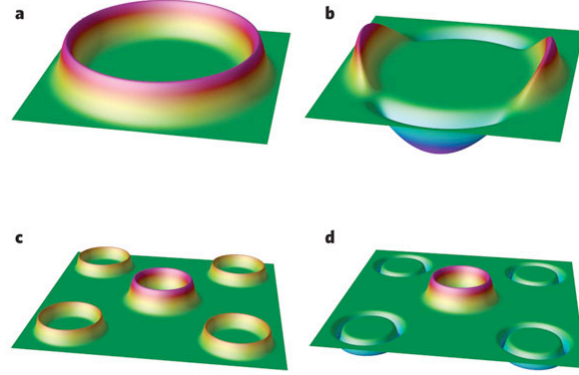
Figure 1.2 A schematic representation of the superconducting gap with sign change in gap function between different Fermi surface: conventional s-wave gap(**a**); d-wave(**b**); two-band s-wave with the same sign of the gap function (**c**); $s_\pm$ two-band s-wave with a sign change between in the gap function(**d**). [Mazin [2010]]

responsible for this pairing [Taillefer [2010]].

Because the cuprate systems must be doped to induce superconductivity, we can look at their doping phase diagram to better understand the family. Starting with the parent compound at room temperature we see a Mott insulator and antiferromagnetism once cooled below T_N. As hole doping increases, the T_N decreases and is eventually suppressed to zero. There is a clear gap between the end of the antiferomagnetic domain and the first signs of superconductivity. This gap is a region of spin glass with no long range order. Above some critical concentration, superconductivity appears, first with very low temperatures, moving to higher doping levels the superconducting T_c increases to a maximum at optimal doping . At a temperature above T_c there exists a not well understood pseudo-gap phase extending to almost room temperature. As doping continues to increase, T_c decreases from its peak value, at the same time the pseudo gap phase disappears and is replaced by a normal metal. At some concentration the superconductivity is suppressed and the normal metal persists to zero temperature, see Figure

1.3. As shown in this phase diagram, the superconductivity is formed in close proximity to a magnetically ordered state, which further enhances the likelihood of a magnetically mediated pairing mechanism.
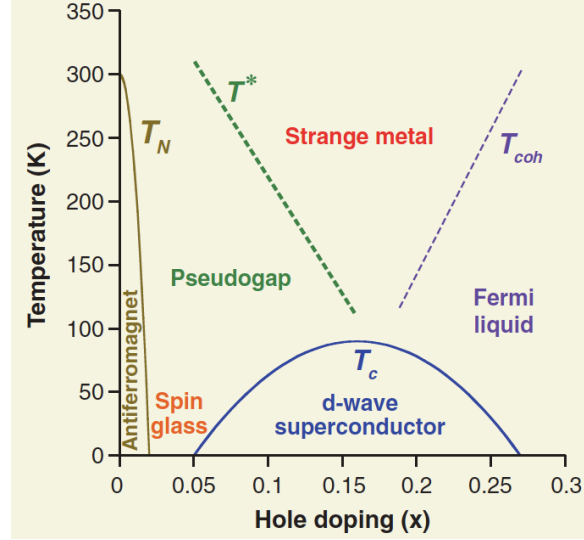
Figure 1.3 Schematic phase diagram representative of a generic cuprate superconductor. [Norman [2011]]

The discovery of superconductivity in Fe based materials by [Kamihara et al. [2008]] set off a scramble to quickly identify whether they are similar to the Cuprates. In general, Fe based superconductors are considered high temperature superconductors with correspondingly high upper critical fields. The superconductivity forms a dome in the doping phase diagram with maximum T_c observed close to a point where magnetism vanishes Fig. 1.4. The proximity to a magnetically ordered state pointed research toward the possibility of a d-wave and of magnetically mediated superconductivity. The iron based superconductors start as paramagnetic metals until they are cold and stripe type antiferromagnetism sets in. As doping is added, the T_N and T_s decreases but the compounds remain metallic. At some concentration superconductivity appears with no gap between the magnetic phase and the superconducting phase. In

some systems there is a documented magnetic order within the superconducting dome. At the edge of the magnetically ordered phase there is a peak in the superconducting transition temperature and then s decreases to zero. If doping continues after superconductivity is suppressed the system will remain in a paramagnetic metallic phase, see Figure 1.4. One major difference between Fe based systems and the Cuprates is seen as we move across the dome, the Cuprates pairing symmetry remains constant from one dome edge to the other. In the case of the Iron based superconductors there have been observations of a changing symmetry as one moves across the dome.
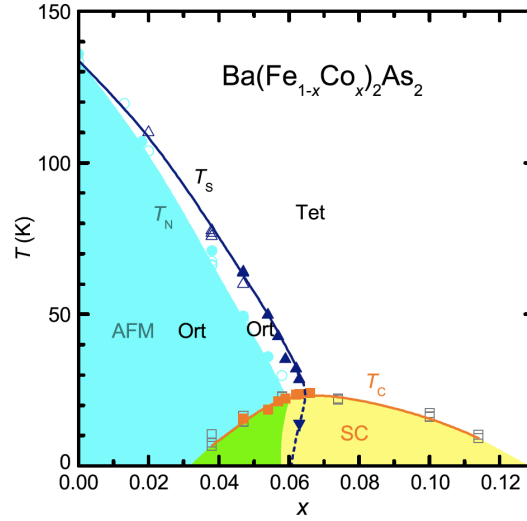
Figure 1.4 Doping phase diagram of Ba(Fe$_{1-x}$Co$_x$)$_2$As$_2$, showing domains antiferromagnetism, and proceeding it orthorhombic distortion.

Several different measurements can be used to identify the pairing symmetry, however in the Prozorov lab we use the functional form of the low temperature London penetration depth. The early studies of London penetration depth on iron based superconductors showed somewhat contradicting results. In 2009 Malone found that the London penetration depth in LaFeAsO$_{1-x}$F$_y$ is exponential in temperature dependence corresponding to a full-gapped sys-

tem[Malone et al. [2009]]. It was theorized that this full gap may not be the standard s-wave but another fully gapped state known as $s_{\pm}$, see fig 1.2, [Mazin [2010]]. On the other hand, Felttcher *et.. al.* found that LaFePO shows a linear temperature dependence suggesting the presence of line nodes similar to d-wave case [Fletcher et al. [2009]]. There have been many follow-up studies trying to identify the underlying gap symmetry in many iron based superconducting compounds. After several years and a lot of effort by several groups a pattern did start to appear.

With the iron based materials requiring doping to become superconducting, it was thought that doping was not only fostering superconductivity but also adds to the scattering and breaking of the Cooper pairs. It is very difficult to quantify the amount of the impurity scattering caused by the doping alone. If we could add a known amount of scattering we could use well known theoretical works to differentiate the underlying pairing symmetries. Anderson showed that for single gap s-wave systems the addition of non-magnetic impurities does not change the superconductivity [Anderson [1959]]. One year later Abrikosov and Gorkov showed that when magnetic impurities are added to single gap s-wave superconductors, they would decrease the T_c and could also change the low temperature penetration depth from $\lambda \sim e^{-\frac{\Delta}{T}}$ to a power law dependence $\lambda \sim T^n$ with *n* as low as 2 [Abrikosov and Gor'kov [1960]]. On the other hand, Hirschfeld and Goldenfeld showed that for the nodal systems, such as d-wave, adding non-magnetic impurities would change $\lambda(T) \sim T$ in the clean limit toward T^2 [Hirschfeld and Goldenfeld [1993]]. It has already been suggested that iron based superconductors may not be single gap s-wave or nodal d-wave but some other gap symmetry such as $s_{\pm}$[Mazin [2010]]. In that case Yunkyu Bang [Bang [2009]] and Vorontsov in [Vorontsov et al. [2009]] showed that the temperature dependence of λ will change from exponential $\lambda \sim e^{-\frac{\Delta}{T}}$ to a power law $\lambda \sim T^n$ with exponent n as low as 1.6 in the dirty limit.

This naturally sets up an experiment that can be preformed, if a suitable way to add a

known amount of impurity scattering can be found. One suggestion from the days of cuprate studies was to use heavy-ion irradiation [Zhu et al. [1993]] to control the number of defects added. The first study of irradiated Fe based superconductors was preformed by Kim *et. al.* [Kim et al. [2010]]. The authors found that for Ba(Fe$_{1-x}$Y$_x$)$_2$As$_2$ with Y=Co or Ni not only does the T$_c$ decrease as the dose of heavy-ions increases, but the power-law exponent *n* decreases. The penetration depth study of this thesis extends the work of Kim *et. al.* to higher doses of irradiation and to the over doped edge of the superconducting dome. There were suggestions of an increase in the gap anisotropy as one moves toward the over doped edge [Reid et al. [2010],Martin et al. [2010]]. The works by Reid *et. al.* and Martin *et. al.* also showed a change in the gap structure between parallel and perpendicular to the c-axis [Reid et al. [2010], Martin et al. [2010]].

Knowing the works of Reid *et. al.* and Martin *et. al.* we started looking for a complementary way to observe this difference in the direction of possible nodes in the gap of Fe bases superconductors. There was a previous work done on the anisotropy of the upper critical field in Ba(Fe$_{1-x}$Co$_x$)$_2$As$_2$[Altarawneh et al. [2008]] showing that the anisotropy of the upper critical field, $\gamma_H = \frac{H_{c2,\parallel}}{H_{c2.\perp}}$, changes greatly between the under and over doped sides of the superconducting dome. We choose to not only measure the the upper critical field for both principal crystallographic directions but to study in detail the angular dependence which can reflect the superconductor modulation. We used the theoretical works of Kogan and Prozorov [V.G. Kogan [2012]] to understand the underlying gap structure.

In Fe-based superconductors, the states at the Fermi energy mostly come form the orbitals of Fe. Therefore doping by Fe substitution with other transition metals (Co, Ni) can be accompanied by the highest disruption of the electronic system and strong scattering. Doping into the alternative sites (Ba and As) does not bring as much scattering and allows for cleaner materials. In this thesis I studied the superconducting gap structure of optimally doped SrFe$_2$(As$_{1-x}$P$_x$)$_2$ and compared its properties with those of the transition-metal doped systems. We additionally

lowered the scattering rate in P-doped substantially by low-temperature annealing.

CHAPTER 2. Experimental techniques

2.1   The tunnel diode resonator circuit as a probe of the London Penetration depth

The tunnel diode resonator (TDR) circuit operates as a simple extension of a LC tank circuit. If an ideal inductor and capacitor are connected they will oscillate forever with no loss of energy. However, all real components have some resistive loss. If a negative resistance equal to the resistance of the components of the oscillator were added in parallel with this circuit these losses could be sompensated. This negative resistance is what is gained by the use of the tunnel diode. When an appropriate bias voltage is added to a tunnel diode a region of differential negative resistance occurs (see fig 2.1). A negative resistance is defined as an increase in voltage generating a decrease in current; see figure 2.1. The tunnel diode biased to this region acts as an *ac* power source and compensates for losses in the oscillating components. While tunnel diode driven oscillators can operate at frequencies well into the microwave region our system is tuned to operate at 14MHz.

To allow for the most stable operating frequency and the most accurate measurements possible, the experiment circuit used in our lab, seen in Fig 2.2, consists of an oscillator and two built in filters. The voltage divider created by R_1 and R_2 allows for the room temperature control box to establish the proper dc bias voltage across the diode. If R_1 is large enough, it acts as an additional *rf* filter. The capacitor C_B acts to filter out frequencies in the range of the 14 MHz resonance frequency. The final capacitor C_p restricts the amount of the *ac* power allowed back up to the bias control box and other room temperature electronics.   As can be seen in Fig 2.2
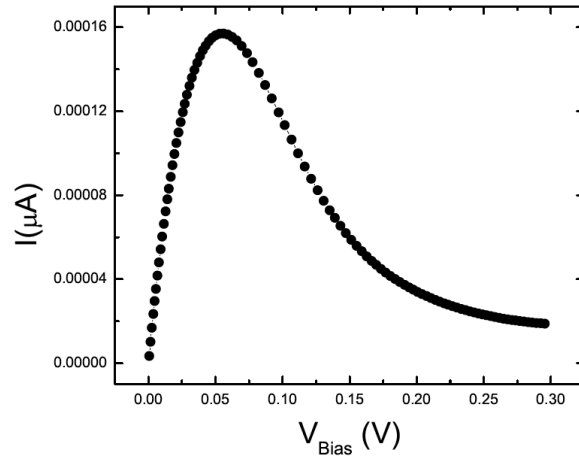
Figure 2.1   I-V curve of a diode used in the Prozorov lab. The region of negative differential
resistance compensates for a increase in V with a corresponding decrease in I.
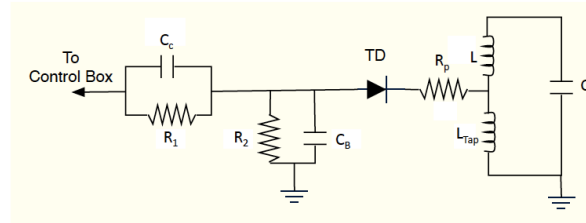
Figure 2.2   TDR Circuit diagram. (Vannette 2008)

there are two inductors labeled L and L_{Tap}. The Tap coil is chosen to be approximately 1/3 the

inductance of the sample inductor. The Tap coil is used to kill upper harmonics created in the

LC circuit. The final piece of the experimental circuit is the parasitic resistor R_P, which kills

possible oscillations created between the capacitance of the diode and the Tap coil.

The TDR circuit is optimized for the use in the temperature range below 30K. After much

experimenting, it was found that keeping the circuit at 5K gives the best frequency stability.

Our circuit is split into 3 segments and mounted into a machined block of copper that was

then gold platted. Using the proper proportional-integral-derivative (PID) control setting on

the temperature controller we are able to achieve temperature accuracy of (5.000 ± 0.001)K. With this level of temperature control we are able to achieve a frequency stability of .02Hz on top of a 14MHz signal.

With an optimized circuit in place we now need to go from changes in the resonate frequency of our circuit due to the presence of the sample in the measurement coil to changes in the value of the London Penetration depth ($\Delta\lambda$). The empty coil frequency can be written as Eq. 2.1.

$$f_0 = \frac{1}{2\pi\sqrt{LC}} \tag{2.1}$$

Here L is the inductance of the empty coil and C is the capacitance of the tank capacitor. The inductance of the coil can be expressed in terms of the magnetic flux in the inductor, with H being the magnetic field inside coil produced be the circuit and V_c is the volume of the coil.

$$\Phi \approx HV_c \tag{2.2}$$

The textbook definition of the inductance L can then be written as

$$L = \frac{d\Phi}{dI} \tag{2.3}$$

If we now place the sample inside the coil the change in frequency Δf becomes

$$\Delta f = \frac{1}{2\pi\sqrt{(L+\Delta L)C}} \tag{2.4}$$

The square root can be expanded using a binomial expansion to find a direct relation between Δf and ΔL

$$\frac{\Delta f}{f_0} \approx -\frac{1}{2}\frac{\Delta L}{L_0} \tag{2.5}$$

L is still determined by the flux through the coil. Now with the sample in place we need to subtract its volume form Φ in Eq. 2.2 but add back in the sample volume V_s multiplied by B the magnetic field in the sample.

$$\Phi' = H(V_c - V_s) + BV_s \tag{2.6}$$

The magnetic field inside the sample is the sum of the applied magnetic field (H) from the TDR circuit and the magnetization M of the sample itself.

$$B = H + 4\pi M \tag{2.7}$$

If we now plug this back into Eq. 2.6 we are left with the total flux inside the coil.

$$\Phi' = HV_c + 4\pi V_s M \tag{2.8}$$

The total inductance of the coil with the sample in place can be written as

$$L' = \frac{d\Phi'}{dI} = \frac{d\Phi'}{dH}\frac{dH}{dI} = \frac{(dHV_c)}{dI} + 4\pi V_s \frac{dM}{dH}\frac{dH}{dI} = L + \Delta L \tag{2.9}$$

This will let us relate ΔL to the magnetic susceptibility χ of the sample.

$$\frac{\Delta L}{L} = \frac{4\pi V_s}{V_c}\chi \tag{2.10}$$

Therefore $\Delta f/f$ can be directly related to χ

$$\frac{\Delta f}{f} \approx \frac{4\pi V_s}{V_c}\chi \tag{2.11}$$

Now we have to relate χ to the London penetration depth ($\Delta\lambda$). In the simplest case of a

spherical sample with s-wave symmetry λ is defined as

$$\lambda = \frac{1}{H_0} \int_0^\infty B(x)\,dx \tag{2.12}$$

In this case B(x) is the magnetic field inside the sample and H_0 is the field at the interface of the semi-infinite sample. When the real size of the sample is taken into account, we need to account for demagnetization effects. In 2000 R. Prozorov published a model that would relate the dynamic magnetic susceptibility χ to the in-plane magnetic penetration depth λ_{ab}. [Prozorov et al. [2000a]] The model works in the limit of thin slab single crystals with the field parallel to the crystallographic c-axis, perpendicular to the slab. The generalized expression in this model can be written as,

$$-4\pi\chi = \frac{1}{1-N}\left[1 - \frac{\lambda_{ab}}{R}\tanh\left(\frac{R}{\lambda_{ab}}\right)\right] \tag{2.13}$$

The slab sample has a thickness of 2d in the x-direction, width 2w in the y-direction and considered infinite in the z-direction, with the field applied in the y-direction. N represents the effective demagnetization factor. Written in this form R is an effective dimension that is used to map the dimensions of the sample under study with the penetration depth. The original and to this point most successful mapping has been for rectangular samples of dimension $2a \times 2b$ with $b\,a$ and thickness written as 2d. For the most successful mapping R can be written as,

$$R \sim \frac{w}{2\left[1 + \left[1 + \left(\frac{2d}{w}\right)^2\right]\arctan\left(\frac{w}{2d}\right)\right]} \tag{2.14}$$

with

$$w = \frac{ab}{a+b} \tag{2.15}$$

For a physical sample R$>>\lambda_{ab}$, from this it is clear that the $\tanh\left(\frac{R}{\lambda_{ab}}\right) \to 1$ plugging this

information into equation 2.13 and then χ into 2.11 we get.

$$\lambda_{ab}(T) - \lambda_{ab}(T_{min}) = \frac{2V_c R(1-N)}{f_0 V_S}[\Delta f(T_{min}) - \Delta f(T)] \equiv G[\Delta f(T_{min}) - \Delta f(T)] \quad (2.16)$$

T_{min} represent the base temperature of the experiment, in the case of the ^3He cryostat this is approximately 0.5 K. The proportionality factor G can be determined in two different ways. The simplest one, which is used in our lab is to measure frequency shift when the sample is physically removed from the coil at base temperature. In the ^3He cryostat we have a simple micrometer that allows for the sample and sample holder to move fully out of the coil. With this method the full frequency change at the base temperature can be measured and directly used as f_0. The only complication comes from the magnetic susceptibility in the sapphire rod used to hold the sample. At temperatures $\sim 0.5K$ sapphire is a paramagnet and contributes on a very small change in frequency on the order of 148Hz which has been measured in a background measurement.

If the sample cannot be removed from the coil, the normal state skin depth may be used to convert from changes in frequency to changes in the penetration depth. The general expression for the normal state skin depth is given as.

$$\delta = \sqrt{\frac{2\rho}{\mu\omega}} \quad (2.17)$$

The equation for the change in the resonance frequency of the circuit due to changes in the normal state skin depth in the presence of a small *ac* magnetic field is

$$\frac{\Delta f}{f} = \frac{V_s}{2V_c}\left[1 - Re\left[\frac{\tanh(\alpha c)}{\alpha c}\right]\right]. \quad (2.18)$$

The complementary equation relating the same change in frequency to the superconducting penetration depth is

$$\Delta\left(\frac{1}{Q}\right) = \frac{V_s}{V_c}Im\left[\frac{\tanh(\alpha c)}{\alpha c}\right] \quad (2.19)$$

For both these equations c is the thickness of the given sample. On the other hand α is different for different materials. For a normal metal α is given by

$$\alpha = \frac{(1-i)}{\delta} \tag{2.20}$$

and for a superconductor α is given by

$$\alpha = \frac{1}{\lambda}. \tag{2.21}$$

For the calibration we need to relate the $\frac{\delta f}{f_0}$ and $\delta\left(\frac{1}{Q}\right)$ to zero magnetic penetration depth. This is straight forward in the first case $\delta\left(\frac{1}{Q}\right) = \Delta\left(\frac{1}{Q}\right)$ and in the frequency domain $\frac{\delta f}{f_0} = \frac{\Delta f}{f_0} - \frac{V_s}{2V_c}$. This gives in the case of a normal metal

$$\frac{\delta f}{f} = \frac{V_s \delta}{4V_c c} \tag{2.22}$$

and in the case of a superconductor

$$\frac{\delta f}{f_0} = \frac{V_s \lambda}{4V_c c}. \tag{2.23}$$

These last two equations give enough information to calibrate the full change in frequency at T_c to the change in the magnetic penetration depth from base temperature to T_c.

2.2 Heavy Ion Irradiation

All heavy ion irradiation for this work was preformed at the Argonne National Laboratory in the Argonne Tandem Linear Accelerator System (ATLAS). At ATLAS Lead ions $^{208}Pb^{56}$

were used to irradiated these samples. Prior to being irradiated, all samples where character-ized and measured using the TDR setup in ^{3}He cryostat. Samples were mounted on copper foil using conductive carbon paste. The sample mounts were then mounted on a aluminum frame to be mounted in the vacuum chamber. The chamber and the samples were at ambient temper-ature. The aluminum frame can move vertically without opening the chamber. This gives the ability to move samples in and out of the beam. Along with vertical motion, the frame has the ability to rotate a full 360° in situ. For this work the rotation capability was not used. To en-sure the uniform exposure of all samples in the beam, one of the aluminum rungs of the ladder setup is covered with a piece of reactive film. The film can be viewed both while the system is in vacuum and again after the run. The beam was collimated to make a 1.0 cm diameter circle, the most uniform region was a 3.0 mm circle. With the beam properly collimated the next thing needed is to know the beam current. With the aluminum frame lowered the beam fell on a copper cup that was to measure the current. The currents measured for these irradiation runs were on the order of 400 pA. The time needed for a particular dose of irradiation can be calculated as

$$n = \frac{tI_{e^-}}{nQqA} \tag{2.24}$$

In this case Q is the charge of the ion, q is the charge of the electron, A is the area of the collimated hole, I_{e^-} is the measured beam current, and t is the exposure time in seconds for the sample is in the beam. If n represents the number of columnar defects, for a typical exposure it is 10^{14} defects/m^2. For a sample of size .5 mm x .5 mm this is $\sim 10^7$ defects created in the sample. It is a convention, from the study of vortex properties, to refer to the number of defects in reference to the matching field that would penetrate the sample if each defect held a single vortex. The conversion between defects the matching field is straight forward.

$$n = \frac{B(T)}{\Phi_n} \tag{2.25}$$

With the field measured in Tesla and Φ_n is equal to the 1 flux quanta.

$$\Phi_n = 2.07 * 10^{-15} \frac{T}{m^2} \tag{2.26}$$

Samples for this study were irradiated with 6 T for the x=0.108 sample and 6.5 T for the x=0.127 sample. As has been discussed before irradiation with heavy-ions produces large, nearly 5 nm, diameter columnar defects propagating through the whole sample thickness. For heavy-ion irradiation done at Argonne with energy of 1.56GeV the ions can penetrate up to 60-70 μm . These values calculated from a commercially available software package and are slightly different for different materials and different ions.

2.3 Measuring the absolute value of λ_{ab}

In the section 3.1 the tunnel diode resonator technique (TDR) was discussed as a tool to measure the change in the London penetration depth $\Delta\lambda(T)$ between the base temperature of the measurement system and the superconducting transition temperature T_c. While $\Delta\lambda(T)$ can be used to determine the presents of noes in the gap, theoretical calculations need determination of a superfluid density $\rho_s = [\lambda(0)/\lambda(T)]^2$, which require the absolute value of the London penetration depth $\lambda(T)$. A method was developed to measure $\lambda(0)$ by R. Prozorov for the use on cuprate superconductors [Prozorov et al. [2000b]] then translated for use on pnictide materials by R. T. Gordon and R. Prozorov [Gordon et al. [2010]]. This method requires the sample to be coated with a thin layer of a referance superconductor with a $T_{c,coating} << T_{c,sample}$ and a known $\lambda(0)$. The coating layer must be thin enough so that when placed in an inductor coil with resonate frequency of 14 MHz the rf skin depth is much greater than the layer thickness. This thin layer of the coating material is nearly invisible to the ac magnetic field and therefore does not affect the measurement above the T_c of the coating material. Along with this requirement the coating material needs to also be thick enough to screen the field below T_c of Al layer. With these and other requirements in mind R. Prozorov [Prozorov et al. [2000b]] choose Aluminum with a $T_c \approx 1.2\ K$.

To understand this technique on a more quantitative level we need to start with considering

an Al coated sample inside the inductor coil of the TDR circuit. We will take the thickness of the coating material d_{Al}, an applied *ac* magnetic field will be taken as

$$\overrightarrow{H}(\mathbf{r},t) = H_0(\mathbf{r})e^{i\omega t}\hat{y} \tag{2.27}$$

Here the $\hat{y}$ direction is taken to be along the axis of the coil and perpendicular to the interface between the coating and sample. When at the base temperature both materials are in the superconducting state and the London equation can be written as

$$\nabla^2 \mathbf{H} = \frac{1}{\lambda^2}\mathbf{H} \tag{2.28}$$
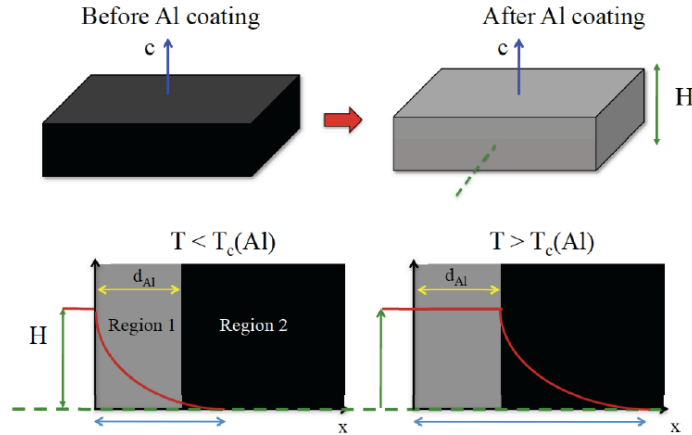
Figure 2.3 Schematic diagram of sample before and after Al coating. [Gordon [2011]]

To go from λ_{eff} to $\lambda(0)$ we need to use a more realistic example. The sample used in this work have been coated with a layer of Aluminum at the University of Illinois in the group of R. W. Geaneta. The coating thickness was measured using an SEM and found to

be $d_{Al} = 1000 \pm 100 \text{Å}$. To ensure the thickness is small enough not to screen the rf once the Al is in the normal state, we need to calculate its skin depth. The skin depth equation Eq. 2.17 given in section 3.1 needs not only the ω but ρ. For Aluminum just above T_c $\rho \approx 10\mu\Omega$. The frequency for this TRD circuit $\omega = 2\pi(14MHz)$. This gives a skin depth $\delta = 75\mu m$, much larger than the coating thickness, which will make the Al coating transparent to the frequency once above the T_c of Al. If we take an example of a superconductor with $\Delta\lambda_{sample}(T) = CT^n$ and a value of n$\approx$3 and a base temperature on the system $T_{min} \approx 0.5\ K$ we can take the inductance L to be

$$L = \Delta\lambda_{eff}\left(T_c^{Al}\right) - \Delta\lambda_{eff}\left(T_{min}\right). \tag{2.29}$$

Using this for the effective lambda for our system we get

$$\lambda_{eff} = \lambda_{Al}\left(T\right)\left(\frac{\lambda_{sample}\left(T\right) + \lambda_{Al}\left(T\right)\tanh\frac{d_{Al}}{\lambda_{Al}(T)}}{\lambda_{Al}\left(T\right) + \lambda_{sample}\left(T\right)\tanh\frac{d_{Al}}{\lambda_{Al}(T)}}\right) \tag{2.30}$$

On the other end of the measurement at $T = T_{c,Al}$ the coating does not interfere with the rf signal but does contribute to the sample size and therefore λ_{eff}.

$$\lambda_{eff}\left(T_{c,Al}\right) = d_{Al} + \lambda_s ample\left(T_{c,Al}\right) \tag{2.31}$$

As stated before, $\Delta\lambda_{sample}(T) = CT^n$ with this Eq. 2.31 now becomes

$$\lambda_{eff}\left(T_{c,Al}\right) = d_{Al} + C\left(T_{c,Al}\right)^n + \lambda_{sample}\left(0\right) \tag{2.32}$$

To get to a final value we need to be able to accurately evaluate the penetration depth of the Al coating $\lambda_{Al}(T_{min})$. Knowing that Al is a s-wave superconductor we can use the BCS fitting [J. Bardeen [1957], Poole et al. [2007]]

$$\lambda_{Al,BCS}(T_{min}) \approx \lambda_{Al}(0)\left(1 + \sqrt{\frac{\pi\Delta_{Al}(0)}{2k_BT_{min}}}e^{-\frac{\Delta_{Al}(0)}{k_BT_{min}}}\right) = \lambda_{Al}(0)\left(1 + \sqrt{\frac{\pi 0.85T_{c,Al}}{T_{min}}}e^{\frac{-1.7T_{c,Al}}{T_{min}}}\right)$$
(2.33)

For Aluminum $\lambda_{Al}(0) = 500 \pm 100\text{Å}$ [N. W. Ashcroft [1976]]. If we now go back and plug this into Eq. 2.29 we get

$$L = d_{Al} + C\left(T_{c,Al}\right)^n + \lambda_{sam}(0) - \lambda_{Al}^{BCS}(0)\left(\frac{C\left(T_{min}\right)^n + \lambda_{sam}(0) + \lambda_{Al}^{BCS}(0)\tanh\frac{d_{Al}}{\lambda_{sample}(0)}}{\lambda_{sam}(T_{min}) + \left(C\left(T_{min}\right)^n\right)\lambda_{sam}(0)\tanh\frac{d_{Al}}{\lambda_{sam}(0)}}\right)$$
(2.34)

All of these values except for $\lambda_{sample}(0)$ have been measured or calculated. This equation can be rewritten in a vary careful way to be in the form of a simple quadratic to solve for $\lambda_{sample}(0)$.

$$\lambda_{sample}(0) = \frac{-b - \sqrt{b^2 - 4ac}}{2a}$$
(2.35)

The coefficients would need to be

$$a = -\tanh\frac{d_{Al}}{\lambda_{Al}(T_{min})}$$
(2.36)

$$b = \left[L - d_{Al} - C\left(T_{c,Al}\right)^n - C\left(T_{min}\right)^n\right]\tanh\frac{d_{Al}}{\lambda_{Al}\left(T_{min}\right)} \tag{2.37}$$

$$c = -a\left[(L - d_{Al})C\left(T_{min}\right)^n - C^2\left(T_c^{Al}T_{min}\right)^n + \lambda_{Al}^2\left(T_{min}\right)\right] + \lambda_{Al}\left(T_{min}\right)\left[L - d_{Al} - C\left(T_c^{Al}\right)^n + C\left(T_{mn}\right)^n\right] \tag{2.38}$$

If L is taken to be L≈0.33μm we find values in the range of $\lambda_{sample} \approx 300nm$. This value falls right in line with values obtained from complimentary measurements [Williams et al. [2010],Luan et al. [2010],NakaJima et al. [2010]]

Use of the Al coating technique in our group has produced reliable results of the absolute value of the London penetration depth in iron based materials see [Gordon et al. [2010],Kim et al. [2010],Murphy et al. [2013]] for details

2.4 Angular Dependent H$_{c2}$

Upper critical field was determined from the standard 4-probe resistivity measurements. Samples for in-plane resistivity, ρ, measurements were cleaved with a razor blade into rectangular strips with typical dimensions, $2 \times (0.1 - 0.3) \times (0.03 - 0.1)$ mm^3 and the long side corresponding to the tetragonal a-axis. All sample dimensions were measured with an accuracy of about 10%. Contacts to the samples were made by attaching silver wires using ultra-pure
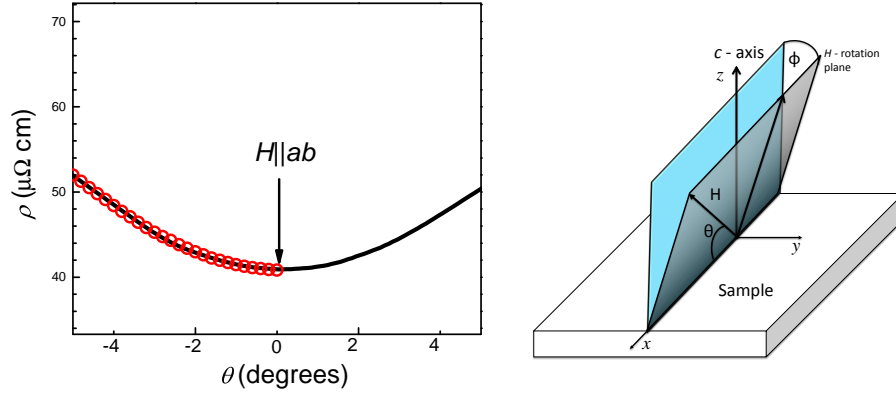
Figure 2.4 During experiments in single axis rotation system of 35 T magnet, the direction of magnetic field was aligned parallel to the conducting plane by resistivity measurements in field H slightly lower than $H_{c2\parallel}$, in which sample resistance shows strong angular dependence, black line in the left panel. The curve was measured in one-sided motion of the rotator to avoid backlash, with deep minimum corresponding to $H \parallel ab$ or $\theta=0$ condition. The red open symbols show alignment measurements, taken in a second angular sweep of the same rotation direction, and stopped at $\theta=0$. H and T sweeps were used to determine the phase diagrams in $H \parallel ab$ condition, and then magnetic field angle θ with respect to the plane was changed by continuing rotation of the sample in the same direction as during alignment. Because the orientation of the sample in the third direction, perpendicular to the rotation plane, was set by eye, there may exist non-zero angle φ between the field-rotation plane and the plane of the normal to the sample. In most cases this angle should be less than 5°.

tin, resulting in an ultra low contact resistance (less than 10 $\mu\Omega$) [Tanatar et al. [2010a]]. Resistivity measurements were made using a standard four-probe technique, producing the $\rho(T)$ curves as shown in Fig. 4.1. After initial preparation, samples were characterized in PPMS system, and then glued by GE-varnish to a plastic platform, fitting single axis rotator of the 35 T DC magnet in National High Magnetic Field Laboratory in Tallahassee, Florida. Sample resistance was checked after mounting and found to be identical to the initial value. High-field measurements were made in He-cryostat with variable temperature control inset (VTI) allowing for temperatures down to 1.5 K.

The stepping motor driven rotator enabled *in situ* rotation with 0.05^o resolution around a horizontal axis in single axis rotation system of vertical 35 T magnetic field. During this rota-

tion the direction of magnetic field with respect to the crystal stays in a plane of rotation, see Fig. 2.4. We can precisely align the direction of the magnetic field parallel to the sample plane within the rotation plane, defined as $\theta=0$, using angular dependence of resistivity, measured in magnetic field slightly below $H_{c2\parallel}$. This alignment is illustrated in Fig. 2.4. In an ideal case of the second sample axis coinciding with the rotation axis, field-rotation plane should contain c-axis of the sample. There may been non-zero uncontrolled angle φ between the field-rotation plane and the plane of the normal to the sample, see Fig. 2.4. We estimate that $\varphi < 5°$.

2.5 Sample growth and characterization

Single crystals of BaFe$_2$$As$_2$ doped with Co were grown from a starting load of metallic Ba, FeAs and CoAs, as described in detail elsewhere [Ni et al. [2008]]. Crystals were thick platelets with sizes as big as $12 \times 8 \times 1$ mm^3 and large faces corresponding to the tetragonal (001) plane. The actual content of Co in the crystals was determined with wavelength dispersive electron probe microanalysis and is the x-value used throughout this text. The two compositions studied were x=0.108 ($T_c \approx$16 K) and x=0.127 ($T_c \approx$8 K), from the same batches used in previous penetration depth [Gordon et al. [2009a, 2010]] and thermal conductivity [Tanatar et al. [2010c],Reid et al. [2010]] studies. They were on the overdoped side of the doping phase diagram (see inset in Fig. 4.1), notably above optimal doping level x_{opt}=0.07 (T_c $\approx$23 K).

Single crystals of SrFe$_2$(As$_{1-x}$P$_x$)$_2$ were grown using the self-flux method [T. Kobayashi [2012]]. Samples were characterized by x-ray, magnetization and transport measurements and the composition was determined using EDX analysis, which yielded $x =$0.35. For London penetration depth measurements samples were selected from different batches by measuring the transition curves and finding the sharpest transition. The best samples were cut to a typical sample size of $0.5 \times 0.5 \times (0.02\text{-}0.1)$ mm^3. Annealing was shown to improve T$_c$ from 31 K to 34.8 K and to increase the residual resistivity ratio, RRR=R(300 K)/R(T_c) from 4.5 to 6.4.

Annealing at 500C did not affect sample composition within accuracy of EDX measurements, so its effect is mainly to reduce the density of thermodynamically metastable defects formed at high growth temperature, predominantly pairs of vacancies and interstitial atoms [Liu et al. [2013]]. A lesser increase of T_c from 30 K to 31 K and of RRR from 4.8 to 5.2 after the annealing was reported for close to the optimal doping ($x = 0.32$) BaP122 samples [Nakajima et al. [2012]], see insets in Fig. 3.6. Furthermore, if we extrapolate linearly the resistivity curves to $T = 0$, we obtain RRR(0) = 10.2 and 15.1 for as-grown and annealed SrP122, and RRR(0) = 7.1 and 8.1 for as-grown and annealed BaP122, respectively. By these measures, SrP122 appears to be cleaner than BaP122.

CHAPTER 3.   Penetration depth measurements

3.1   Introduction

In this chapter I will present London penetration depth data on two iron based super-conducting compounds Ba(Fe$_{1-x}$Co$_x$)$_2$As$_2$ with two Co dopings and SrFe$_2$(As$_{1-x}$P$_x$)$_2$. The two concentrations of Ba(Fe$_{1-x}$Co$_x$)$_2$As$_2$ are x=0.108 and x=0.127 respectively 3.1 and the SrFe$_2$(As$_{1-x}$P$_x$)$_2$ has x=0.35. For both materials the London penetration depth was measured using the tunnel diode resonator technique (TDR). For the Ba(Fe$_{1-x}$Co$_x$)$_2$As$_2$ materials heavy-ion irradiation was used to add controlled damage to the crystallographic lattice, following this the samples were measured again using (TRD). The SrFe$_2$(As$_{1-x}$P$_x$)$_2$ material was measured in the as grown state (T$_c$~25 K), and in the annealed state (T$_c$~35 K). Both types of samples were remeasured after Al coating.

3.2   Ba(Fe$_{1-x}$Co$_x$)$_2$As$_2$

In Fig. 3.2 we show the temperature-dependent variation of the London penetration depth in pristine samples of BaCo122 with $x = 0.108$ (Top panel) and $x = 0.127$ (bottom panel). Due to rather low $T_c \approx 8\,K$ of the sample with $x = 0.127$, measurements down to T$\approx 0.5\,K$, the base temperature of our ^{3}He system, do not cover a broad enough range to give reliable power-law analysis. We extended the temperature range by taking the data in a dilution refrigerator down to $\approx 0.05\,K, T_c/160$. The data sets taken in the two systems perfectly match in the overlapping range 0.5 to 3.5 K providing support for the reliability of the measurements. It is clear from the inspection of the raw data, that the temperature variation of the London penetration depth

is much stronger than the exponential variation expected in a full-gap superconductor. In fact the dependence is close to T^2, as shown in Fig. 3.3, in which the data for two compositions are plotted vs. $(T/T_c)^2$ which is similar to the earlier data by Grordon *et.al.*[Gordon et al. [2009a]]. As can be seen from Fig.3.3, the exponent *n* is larger for closer to the optimal doping composition x=0.108. Using a power-law fit over a temperature range up to $T_c/3$, we obtain $n = 2.5$ for sample with $x = 0.108$ and $n = 2.0$ for $x = 0.127$. These values and their change with doping follow general trend in iron-pnictides [Cho et al. [2012]]. In BaCo122 this evolution is in line with the results of thermal conductivity[Tanatar et al. [2010c],Reid et al. [2010]] and heat capacity[Bud'ko et al. [2009]] studies.

Figure 3.1 Temperature dependent electrical resistivity of reference samples *x*=0.108 and *x*=0.127 and of the irradiated sample of *x*=0.127. The irradiated sample *x*=0.127 is the same sample as used in penetration depth measurements, with contacts attached. Inset shows the doping phase diagram for BaCo122 with position of the samples used in this study.

3.3 Heavy ion irradiated Ba(Fe$_{1-x}$Co$_x$)$_2$As$_2$

Figure 3.4 shows the London penetration depth from base temperature to $\sim T_c/3$ in the sample *x*=0.108 (Top panel) before (black curve) and after 6.5T irradiation (red curve). Inset

Figure 3.2 Low temperature London penetration depth $\Delta\lambda$(T) for samples of Ba(Fe$_{1-x}$Co$_x$)$_2$As$_2$ with x=0.108 (Top panel) and x=0.127 (bottom panel). Data were taken in both ^{3}He-cryostat (down to $\sim$0.5 K, black curves) and in a dilution refrigerator ($\sim$0.05 K$< T <$3 K, red curve), showing good matching between the data sets taken in two systems and the robustness of the power-law dependence.

shows the data for the whole temperature range, revealing small but clear decrease of T_c. Irradiation significantly increases the total $\Delta\lambda(T)$ change from base temperature to $T_c/3$. The similar data for sample x=0.127 in pristine (black line) and 6 T irradiated (red line) states are shown in the bottom panel of Fig. 3.5. The T_c decrease in sample x=0.127 is somewhat larger than in sample x=0.108, and similarly, overall change in the penetration depth to $T_c/3$ is larger as well.

In standard analysis of the penetration depth in single gap superconductors, the power-law fit is done in the range from base temperature to $T_c/3$, over the temperature range in which

Figure 3.3 Low temperature London penetration depth $\Delta\lambda(T)$ for samples of Ba(Fe$_{1-x}$Co$_x$)$_2$As$_2$ with x=0.108 (green and blue curves) and x=0.127 (black and red curves) plotted vs. square of the reduced temperature, $(T/T_c)^2$. Linear plot for x=0.127 shows that the dependence is very close to T^2, consistent with more detailed fitting analysis using floating fitting range, see figures . 3.4 and 3.5 below. Clear deviations for sample x=0.108 suggest $n > 2$.

the superconducting gap itself can be considered as constant. This assumption may be not valid for multi-band superconductors, in which case the high-temperature end of the fitting range can be reduced proportionally to the ratio of the smaller and larger gaps. Since this ratio is *a priori* unknown, we varied the high temperature range of the fit. We used a power-law function $\Delta\lambda(T) = AT^n$ and determined n and A as a function of the high-temperature end of the fitting range, always starting fit at the base temperature. The results of this fitting analysis for pristine and irradiated samples are shown in Fig. 3.4, for samples with x=0.108 sample and Fig. 3.5 for the x=0.127 sample. The top panels show evolution of the exponent n and the bottom panels show evolution of the pre-factor A.

The results of the fitting analysis, Fig. 3.4 show that for sample with x=0.108 the exponent n weakly depends on the fitting range, changing from 2.7 to 2.6. In irradiated samples the exponent decreases to n=2.2 for $T_c/4.5$, and slightly increases to 2.3 for $T_c/3$. The decrease of the exponent with irradiation is not expected in either s^{++} or d-wave states, it is a hallmark signature of the $s_\pm$ pairing.

Figure 3.4   Left: Modification of the temperature dependent London penetration depth, $\Delta\lambda(T)$, with heavy ion irradiation in samples with $x = 0.108$. Black curves show pristine samples, red- irradiated with matching fields of 6.5 T. Insets show variation of London penetration depth in the whole range up to T_c. Right: Dependence of the fitting parameters, n (Top panels) and A (bottom panels), of the power-law function, $\Delta\lambda = AT^n$, on the temperature of the high-temperature boundary of the fitting interval. Data are shown for pristine (black squares) and irradiated (yellow-brown circles) sample with $x=0.108$

The effect of irradiation is even more dramatic in sample with $x=0.127$ see figure 3.5. Here the exponent in the pristine sample is $n=2.0$, a value possible to explain in both dirty d-wave and dirty $s_\pm$ scenarios [Hirschfeld and Goldenfeld [1993], Gordon et al. [2009b]]. In the former the exponent is expected to be insensitive to increase of scattering, in the latter it is expected to decrease further down to about 1.6. As can be clearly seen, irradiation decreases n to 1.8, suggesting an increase of anisotropy. Simultaneously, the pre-factor in these samples also increases after irradiation, clearly showing the appearance of excess quasi-particles.

3.4   Absolute Value of the Penetration depth in $SrFe_2(As_{1-x}P_x)_2$

For London penetration depth measurements samples were selected from different batches by measuring the transition curves and finding the sharpest transition. The best samples were cut to a typical sample size of $0.5 \times 0.5 \times (0.02\text{-}0.1)$ mm^3. Annealing was shown to improve T_c from 31 K to 34.8 K and to increase the residual resistivity ratio, RRR=R(300 K)/R(T_c)

Figure 3.5   Left: Modification of the temperature dependent London penetration depth, $\Delta\lambda(T)$, with heavy ion irradiation in samples with $x = 0.127$. Black curves show pristine samples, red- irradiated with matching fields of 6 T. Insets show variation of London penetration depth in the whole range up to T_c. Right: Dependence of the fitting parameters, n (Top panels) and A (bottom panels), of the power-law function, $\Delta\lambda = AT^n$, on the temperature of the high-temperature boundary of the fitting interval. Data are shown for pristine (black squares) and irradiated (yellow-brown circles) sample with x=0.127 (right).

from 4.5 to 6.4. Annealing at 500C did not affect sample composition within accuracy of EDX measurements, so its effect is mainly to reduce the density of thermodynamically metastable defects formed at high growth temperature, predominantly pairs of vacancies and interstitial atoms [Liu et al. [2013]]. A lesser increase of T_c from 30 K to 31 K and of RRR from 4.8 to 5.2 after the annealing was reported for close to the optimal doping ($x =$0.32) BaP122 samples [Nakajima et al. [2012]], see insets in Fig. 3.6. Furthermore, if we extrapolate linearly the resistivity curves to $T = 0$, we obtain RRR(0) = 10.2 and 15.1 for as-grown and annealed SrP122, and RRR(0) = 7.1 and 8.1 for as-grown and annealed BaP122, respectively. By these measures, SrP122 appears to be cleaner than BaP122.

Figure 3.6 shows the full temperature range variation of the in-plane London penetration depth, $\Delta\lambda(T)$, measured in an as - grown ($T_c = 27$ K) and two annealed ($T_c = 34.8$ K) single crystals of $SrFe_2(As_{1-x}P_x)_2$, $x =$0.35 see [Nakajima et al. [2012]]. The insets show normalized

Figure 3.6 Main pane: In-plane London penetration depth in single crystals of $SrFe_2(As_{1-x}P_x)_2$, $x = 0.35$, in the full temperature range showing one as–grown and two annealed samples. Top inset: shows normalized resistivity, $R(T)/R(300\ K)$ for as-grown and annealed $SrFe_2(As_{1-x}P_x)_2$ (this work) and $BaFe_2(As_{1-x}P_x)_2$ [Nakajima et al. [2012]]. Lower inset: shows the same data zoomed on in the vicinity of T_c.

resistivity, $R(T)/R(300\ K)$ for as-grown and annealed SrP122 (this work) and BaP122 [Naka-jima et al. [2012]] samples. Lower inset shows the data zoomed in the vicinity of T_c. Overall, the resistivity curves for SrP122 and BaP122 are virtually the same showing clear deviation from the Fermi liquid T^2 dependence at all temperatures, indicating proximity to the quantum critical point at the optimal doping [Hashimoto et al. [2012], Carrington [2011], Nakai et al. [2010], T. Kobayashi [2012], Tanatar et al. [2013]].

Figure 3.7 shows the low temperature behavior of the penetration depth for three samples of $SrFe_2(As_{1-x}P_x)_2$. Two of the curves are shifted vertically by 0.06 and 0.12 nm to avoid overlap. The linear temperature dependence is evident. Some rounding off at the low temperatures is due to impurity scattering as was shown for nodal Cuprate superconductors by Hirschfeld and Goldenfeld [Hirschfeld and Goldenfeld [1993]]. Within their model the behavior at low temperatures can be approximated by $\Delta\lambda(T) = At^2/(t^* + t)$ where t^* is a crossover temperature

scale determined by unitary limit impurity scattering. Solid red curves in Fig. 3.7 show best fits to the data resulting in the crossover temperatures $t^* = 0.068$, 0.101 and 0.285 for the three curves from bottom up. The amplitude A also increases from the bottom to the top curve, $A = 88$, 97 and 130 nm, respectively. A straightforward interpretation is that we are dealing with samples with different degrees of scattering from the cleanest (lowest curve) to the dirtiest (top curve) and such assignment is in line with the effect of annealing on resistivity and T_c. Good quality fits to the Hirschfeld - Goldenfeld formula, as shown in Fig. 3.7, would appear to indicate the presence of line nodes. However, this is not sufficient for the determination of the topology of the nodal lines on the multi-band warped Fermi surface. For a full analysis we must determine the superfluid density over the entire temperature range. Knowing the variation of $\Delta\lambda(T)$, the superfluid density is given by $\rho_s(T) = \lambda^2(0)/\lambda^2(T) = (1 + \Delta\lambda(T)/\lambda(0))^{-2}$, so we need to know the absolute value of zero - temperature penetration depth, $\lambda(0)$. To obtain this value we used TDR measurements of Al coated samples[Prozorov et al. [2000a]]. After initial measurement of $\Delta\lambda(T)$ each sample is uniformly coated with Al using magnetron sputtering and then remeasured [Prozorov et al. [2000a], Gordon et al. [2010]]. To ensure a uniform Al film thickness the sample is suspended by a fine wire from a rotating stage inside the sputter deposition chamber. The thickness of the Al layer, d, was measured using focused - ion beam cross-sectioning and imaging in SEM [Gordon et al. [2010]]. In our case $d = 73$ nm is greater than the Al London penetration depth, $\lambda^{Al}(0) = 52$ nm. At $T < T_c^{Al}$, the effective penetration depth is given by:

$$\lambda_{eff}(T) = \lambda^{Al}(T) \frac{\lambda(T) + \lambda^{Al}(T) \tanh \frac{d}{\lambda^{Al}(T)}}{\lambda^{Al}(T) + \lambda(T) \tanh \frac{d}{\lambda^{Al}(T)}} \tag{3.1}$$

where $\lambda(T)$ is the London penetration depth of the material of interest. When Al becomes normal at $T_c^{Al} \approx 1.28$ K, $\lambda_{eff}(T) = d - \lambda(T_c^{Al})$. Extrapolation of $\Delta\lambda(T)$ to $T = 0$ shows that $\lambda(T_c^{Al}) \approx \lambda(0) + 0.7$ nm and by using the BCS s-wave form of $\lambda(T)$ for Al, we can estimate the difference, $L = \lambda(0) - \lambda_{eff}(0)$. Solving numerically Eq. 3.1 we obtain $\lambda(T)$. Considering all the uncertainties, we estimate the accuracy as ± 10 nm.

Figure 3.7 Low - temperature part of $\Delta\lambda(T)$ for the three samples of $SrFe_2(As_{1-x}P_x)_2$, $x =0.35$. Solid lines show the best fits to the Hirschfeld - Goldenfeld model Hirschfeld and Goldenfeld [1993], see text for discussion.

Figure 3.8 illustrates the procedure to estimate the absolute value of $\lambda(0)$. Main panel shows full temperature - range $\Delta\lambda(T)$ for the same annealed sample measured before and after aluminum coating. Evidently, the curves reproduce each other perfectly for $T > T_c^{Al}$ indicating a good repeatability and stability of our measurements. The low - temperature part in the vicinity of the superconducting transition of the aluminum layer is shown in the inset in Fig. 3.8. The curves are offset vertically, so that BCS extrapolation (shown my the solid line) to $T = 0$ gives effective penetration depth of $\lambda_{eff}(T) = d - \lambda(T_c^{Al}) = 21.3$ nm. The difference between the uncoated sample and the coated sample at $T = 0$ gives a rough visual estimate of $\lambda(0) = 271$ nm and the numerical solution of Eq. 3.1 (with the discussed above uncertainty of 10 nm) finally gives $\lambda(0) \approx 275 \pm 10$ nm. Applying the same procedure, we obtained $\lambda(0) = 300 \pm 10$ nm for the as-grown sample, consistent with the assumption of an enhanced pair - breaking compared to the annealed samples. In BaP122 at the optimal doping, $x =0.30$, we obtained a comparable magnitude of $\lambda(0) \approx 330$ nm, but the situation is complicated by the strong doping dependence of $\lambda(0)$ due to the quantum critical point hidden beneath the dome

Figure 3.8 Main panel: full - temperature $\Delta\lambda(T)$ of the same sample of $SrFe_2(As_{1-x}P_x)_2$ be-
fore and after aluminum coating showing that the curves are indistinguishable for
$T > T_c^{Al}$. Inset shows the region of the Al transition. The curves are offset verti-
cally by $\lambda_{eff}(T) = d - \lambda(T_c^{Al})$ providing a rough visual estimate of $\lambda(0) \approx 271$ nm
upon extrapolation of the uncoated sample curve to $T = 0$. Numerical solution of
Eq. 3.1 gives $\lambda(0) \approx 275 \pm 10$ nm.

[Hashimoto et al. [2012]]. Whether the same features exist in SrP122 requires a systematic

doping study.

Combining the results presented in Fig. 3.7 and Fig. 3.8 we can compare the rate of change

of the penetration depth with temperature observed in other clean nodal superconductors with

the current work. In a $d-$wave superconductor with vertical line nodes, the amplitude of the

(T-linear) low - temperature variation of the penetration depth is given by [Xu et al. [1995]]:

$$\frac{d(\lambda/\lambda(0))}{d(T/T_c)} \equiv \frac{d\lambda}{dt} = \frac{2\ln 2}{(d\Delta/d\varphi)_{\varphi \to node}} \tag{3.2}$$

where $(d\Delta/d\varphi)_{\varphi \to node}$ is the slope of the angle - dependent superconducting gap approaching

the node position on the Fermi surface. In the case of $d-$wave pairing, $\Delta(\varphi) = \Delta(0)\cos(2\varphi)$

and $d\lambda/dt = T_c \ln 2/\Delta(0) = \ln 2/2.14 = 0.32$. For YBCO, the measured $d\lambda/dt = 0.33$ [Zhang

et al. [1994], Prozorov et al. [2000a]] and for BSCCO 2212 the observed value is $d\lambda/dt = 0.39$

[Jacobs et al. [1995], Prozorov et al. [2000a]], - both are quite close to the theoretical pre-

diction. In the present case of $SrFe_2(As_{1-x}P_x)_2$, we obtained $d\lambda/dt = 0.28$. For comparison, in $BaFe_2(As_{1-x}P_x)_2$, $d\lambda/dt$ =0.42 and 0.38 for $x = 0.30$ ($\lambda(0)$ =330 nm) and $x = 0.33$ ($\lambda(0)$ =215 nm), respectively Hashimoto et al. [2012]. These values are in a reasonable agreement with the theoretical value of 0.32 showing that the node topology is not much different from that of a standard $d-$wave symmetry.

Figure 3.9 Comparison of the superfluid density, $\rho(T)$, for three samples of $SrFe_2(As_{1-x}P_x)_2$ with the prediction of a two - dimensional $d-$wave pairing (short-dashed line - clean and dashed line - dirty limits) and isotropic $s-$wave (dot-dashed line). We also show $\rho(T)$ for $BaFe_2(As_{1-x}P_x)_2$(gray line, x =0.30, $\lambda(0)$ =330 nm). (Inset) Expanded view of low temperature region.

Figure 3.9 shows experimental superfluid densities constructed with the estimated values of $\lambda(0)$. The data are compared with the expectations for $d-$wave pairing (short-dashed line - clean and dashed line - dirty limits) and isotropic $s-$wave (dot-dashed line). The data are in a complete disagreement with the exponentially saturating $s-$wave curve. Instead, the data show a clear $T-$linear variation at low temperatures. For comparison, the data for $BaFe_2(As_{1-x}P_x)_2$ are also shown by the gray line. The curves for $BaFe_2(As_{1-x}P_x)_2$ and $SrFe_2(As_{1-x}P_x)_2$ overlap at the low temperatures (below T/T$_c$=0.2, see inset), but deviate at higher temperatures. This difference must be due to the difference in the gap magnitudes and anisotropies in these multigap systems, but the low - temperature behavior is determined by the nodal quasiparticles and

the similarity of the data implies that the nodal structure of SrP122 and BaP122 is similar. The deviation from the 2D $d-$wave could be due to geometry of the nodal lines, - perhaps forming the loops in the electron bands [Carrington [2011], Graser et al. [2010], Maiti and Chubukov [2010], Shimojima et al. [2012], Suzuki et al. [2011], Hirschfeld et al. [2011]].

CHAPTER 4.   Measurements of the upper critical field H_{c2}

4.1   Introduction

In this chapter I present upper critical field data for two Iron-based superconducting compounds $Ba(Fe_{1-x}Co_x)_2As_2$ and $Ba(Fe_{1-x}Ni_x)_2As_2$. The two concentrations of $Ba(Fe_{1-x}Co_x)_2As_2$ are x=0.108 and x=0.127 respectively and the $Ba(Fe_{1-x}Ni_x)_2As_2$ are x=0.054 and x=0.072. In both cases the upper critical field was was measured as a function of temperature for fields both parallel and perpendicular to the crystallographic c-axis. For $Ba(Fe_{1-x}Ni_x)_2As_2$ a detailed analysis of the upper critical field as a function of angle between the crystallographic c-axis and the applied magnetic field is given.

4.2 $Ba(Fe_{1-x}Ni_x)_2As_2$

The two compositions studied were on the overdoped side of the phase diagram, slightly overdoped x=0.054 (T_c=16 K) and strongly overdoped x=0.072 (T_c=7.5 K), whereas maximum T_c=19 K is achieved at optimal doping, x_{opt}=0.046 [Ni et al. [2010]], see doping phase diagram in inset in Fig. 4.1.

Samples for in-plane resistivity, ρ, measurements were cleaved with a razor blade into rectangular strips with typical dimensions, $2 \times (0.1 - 0.3) \times (0.03 - 0.1)$ mm^3 and the long side corresponding to tetragonal a-axis. All sample dimensions were measured with an accuracy of about 10%. Contacts to the samples were made by attaching silver wires using ultrapure tin, resulting in an ultra low contact resistance (less than 10 $\mu\Omega$) [Tanatar et al. [2010a]].

Resistivity measurements were made using a standard four-probe technique, producing the $\rho(T)$ curves as shown in Fig. 4.1. After initial preparation, samples were characterized in PPMS system, and then glued by GE-varnish to a plastic platform, fitting single axis rotator of the 35 T DC magnet in National High Magnetic Field Laboratory in Tallahassee, Florida. Sample resistance was checked after mounting and found to be identical to the initial value. High-field measurements were made in He-cryostat with variable temperature control inset (VTI) allowing for temperatures down to 1.5 K.

Figure 4.1 Temperature-dependent resistivity of two samples of $BaFe_{1-x}Ni_xAs_2$ used in this study, with x=0.054 (slightly overdoped) and x=0.072 (strongly overdoped), with doping level indicated with arrows with respect to temperature-doping phase diagram of BaNi122 after [Ni et al. [2010]] shown in the inset. Note pronounced curvature of the $\rho(T)$ for $T > T_c$, typical of overdoped compositions [Doiron-Leyraud et al. [2009]]. Sample resistivity value is defined with accuracy of about 20% due to uncertainty of geometric factors, see Ref. [Tanatar et al. [2009, 2010b]] for details.

In Fig. 4.2 raw ρ(T) data are shown for a set of magnetic elds aligned approximately along the c axis ($\theta = 90°$, top panels) and precisely along the conducting plane (θ=0°, bottom panels), for BaNi122 samples with x = 0.054 and x = 0.072, respectively. We show also the lines corresponding to 20%, 50%, and 80% of the resistivity value immediately above the

transition, $\rho(T_c)$, used as criteria to determine the transition temperature as a function of magnetic eld and construct the phase diagrams, bottom panels (c) of Fig. 4.2. The use of these criteria is justified by small variation of the resistive transition width on application of the magnetic eld, and its independence on the extrapolation, a typical problem for onset and offset criteria.

As can be most clearly seen from the bottom panel of Fig. 4.2, the shapes of the H_{c2} (T) phase diagrams in parallel and perpendicular elds orientations share the same features as found in previous studies of other Fe based systems. The $H_{c2,ab}$ (T) flattens at low temperatures, while $H_{c2,c}(T)$ maintains positive curvature down to the lowest temperatures of our experiment. Both these features are typical for layered materials; see, for example, [See [2000] and Mackenzie et al. [1993]].

In Fig. 4.3 we show eld dependences of in-plane resistivity taken at fixed temperatures with inclination angle θ as a parameter for slightly overdoped sample with x = 0.054 and strongly overdoped sample x = 0.072, respectively. The data analysis will be presented in the next section.

Angular dependence of H_{c2} BaFe$_{1-x}$Ni$_x$As$_2$

$$H_{c2}(\theta) = \frac{H_{c2,ab}}{\sqrt{(\gamma_H^2 - 1)\sin^2\theta + 1}}, \qquad \gamma_H = \frac{H_{c2,a}}{H_{c2,c}}. \tag{4.1}$$

To check if Eq. 4.1 describes our data, instead of commonly used data fitting, as shown in the bottom panels of Fig. 4.3, we used an approach based on data transformation so as to make possible deviations clearly visible. According to[Helfand and Werthamer [1966]] Eq. 4.1, the H_{c2} vs ($\sin^2\theta$) should be a straight line, and in Fig. 4.5 we plot the data this way for samples with x = 0.054 and x = 0.72, respectively. The data show clear deviation from linear trend, irrespective of the criterion of H_{c2} determination from the resistivity data, with the deviation being the strongest close to H$_2$ axis or $\sin^2\theta$ = 1.

To check if the deviation from Eq. 4.1 in Fig. 4.5 can be caused by a finite inclination angle ϕ (see Fig.2.4 for the definition), here we provide the angular dependence of H_{c2} for arbitrary ϕ.

Choosing the cross section of the plane, in which **H** is rotated, with the *ab* crystal plane (see Fig. 2.4) as the *x* axis, we obtain in the crystal frame $\hat{c}$ $\overline{(0,0,1)}$ and the unit vector along the eld $\hat{h} = (\cos\theta, \sin\theta\sin\phi, \sin\theta\cos\phi)$. This gives, for the angle θ_c between the eld and c axis, $\cos\theta_c = \hat{c}\cdot\hat{h} = \sin\theta\cos\phi$. We then obtain for geometry of our experiment

$$H_{c2}(\theta,\phi) = \frac{H_{c2,ab}}{\sqrt{(\gamma_H^2 - 1)\cos^2\phi\sin^2\theta + 1}}. \tag{4.2}$$

It is seen that constant ϕ, as determined by our experimental geometry, does not change the linear relation of H_{c2}^2 $vs\sin 2\theta$, despite changing the magnitude of the variation, vanishing for $\phi = 90°$, corresponding to eld rotation parallel to the conducting plane. Therefore, the linear dependence of H_{c2}^2 on $\sin^2\theta$ is not affected by a misalignment ϕ. The H_{c2} (ϕ) described by Eq. 4.1 is a direct consequence of the linearized Ginzburg-Landau (GL) equation for anisotropic materials at H_{c2}:

$$-(\xi^2)_{ik}\Pi_i\Pi_k\Psi = \Psi, \tag{4.3}$$

where $\Pi = \nabla + 2\pi iA/\phi_0$, A is the vector potential and ϕ_0 is the flux quantum; summation is implied over repeating indices. Both sides of this equation are scalars, so that $(\xi^2)_{ik}$ is a second rank tensor with the standard angular dependence which is reflected in Eq.(4.1).

We note that, in the original papers, the angular dependence, Eq. (4.1), has been derived for single band s-wave superconductors. It has also been recently shown that this behavior is expected for arbitrary Fermi surface, the superconducting gap modulation, and for multiband materials [V.G. Kogan [2012]]. However, this conclusion is achieved assuming the explicit factorization of the pairing potential and order parameter, V (k,k') = V$_0$ $\Omega(k)$ Ω(k') and Δ(T

,k) =Ψ (r,T) Ω(k$_F$). There is no microscopic justification for such factorization in complex superconductors and deviations from Eq. (4.1) can be naturally explained by violation of this procedure. In addition, for iron pnictides the importance of the paramagnetic effects for magnetic fields parallel to the Fe-As plane was suggested to explain the unusual shape of the H$_{c2}$ (T) [Cho et al. [2011],Yuan et al. [2009],Terashima et al. [2009]]. This may also lead to the deviation from Eq. (4.1) with the maximum effect expected at low temperatures and for orientations close to H $||$ *ab* planes.

Clearly, "separable" potentials do not exhaust all possible interactions and, therefore, other forms of the angular dependence H$_{c2}$ (θ) can exist. An example of such a potential has been studied in Ref. 4.4. Such potentials may lead to gradient terms in GL equations different from the standard form Eq. (4.3) and, therefore, different from Eq. (4.1) angular dependencies; see, e.g., [Gor'kov [1987]]. We should also mention deviations from the angular dependence Eq. 4.1 which arise in two- and one-dimensional situations [Tinkham [1996], Lebed and Sepper [2012]]. We therefore may conclude that deviations of the observed angular dependence from H$_{c2}$ of the form (1) (or deviations of H$_{c2}^{-2}$ plotted vs sin^2 θ from the straight line) signal that the coupling potential cannot be written in the separable form. On the other hand, the example of separable potentials (for any Fermi surface and any order parameter symmetry) shows that there is no direct relation between the angular dependence of H$_{c2}$, Fermi surfaces, and order parameter symmetries. However, deviations of H$_{c2}$ (θ) from the form (4.1) may carry such information. To investigate this question further one would need better data on these deviations, in particular, criterion-independent determination of H$_{c2}$, which is hard to achieve in resistive measurements. On the theoretical side, of course, one should go beyond the weak coupling and separable coupling potentials.

Motivated by these considerations, we compile in Fig. 4.4 the published data for various layered materials, analyzed by plotting H$_{c2}^{-2}$ vs sin^2 θ . The data are arranged with decreasing

anisotropy from top to bottom. The most anisotropic materials, staged graphite intercalation compounds (top panel, data from [Iye and Tanuma [1982]]) and layered Sr_2RuO_4 (data from [Deguchi et al. [2002]]), closely follow Eq. (4.1). Interestingly, clear deviations from this behavior in Sr_2RuO_4 , arising due to an unusual limiting mechanism in magnetic fields close to H$||$ *ab*,[Deguchi et al. [2002]] are very difculte to recognize in a limited angular range near θ = 0, as the dependence in the whole range is dominated by the anisotropy of the Fermi surface. On the other hand, two materials in which superconductivity shows strong multiband features, MgB_2 [Kim et al. [2006]] and $NbSe_2$,[Morris et al. [1972]] show distinctly different angular dependences. The H_{c2}^{-2} ($\sin^2 θ$) in pure MgB_2 [Posazhennikova et al. [2002]] shows a downward bent as the field approaches c axis, θ = 90° , similar to but much less pronounced than our observations in BaNi122. On the other hand, doped $Mg(B_{1-x} Al_x)_2$ closely follows the linear H_{c2}^{-2} ($\sin^2 θ$) dependence, Eq. (4.1), which may suggest that doping diminishes multiband effects due to enhanced interband scattering. For pure $NbSe_2$ the $H_{c2}^{-2}(\sin θ)$ plot shows most clear deviations from linearity among all materials, with an upward curvature towards θ = 90°, an opposite trend to pure MgB_2 and BaNi122. The two angular data sets for profoundly multiband iron pnictide superconductors, slightly underdoped BaK12260 and heavily overdoped K122,[Terashima et al. [2009]] generally follow linear dependence despite a profound difference in the superconducting gap structure, nodeless in the former case[Reid et al. [2012a]] and with vertical line nodes in the latter[Reid et al. [2012b]]. Considering that, among all the materials for which we were able to find published H_{c2} (θ), only pure multiband MgB_2 and $NbSe_2$ reveal clear deviations from Eq. (4.1), it is tempting to relate the observed deviations to the multiband superconductivity in the clean limit. This might be quite natural that in these systems the factorization of the pairing potential and of the order parameter does not hold given the complexity of the in- and inter-band interactions. This explanation, however, is not universal, since multiband effects are very pronounced in high purity crystals of $KFeAs_2$, but no clear deviations from Eq. (4.1) are found there. On the other hand, it is hard to consider overdoped BaNi122 as a clean system, since scattering due to substitutional dis-

order, especially on the Fe site, is significant in these compositions. The observation that the deviations from the linear plot in MgB_2 diminish with disorder suggest that the k dependence of the gap magnitude, rather than the multiband nature of the Fermi surface itself, is important for the unusual angular dependence. This conclusion is in line with the recent extension of the Helfand and Werthamer (HW) theory for multi-band superconductors with arbitrary Fermi surfaces. [V.G. Kogan [2012]]

In discussing these results we should keep in mind that, in all cases, except for $Sr_2 RuO_4$, the H_{c2} was measured resistively, so that inevitably its determination is approximate since the resistive transition as a rule has finite width and hence the H_{c2} values depend on a criterion chosen. Finite resistivity in the ux-ow regime (most pronounced in the clean systems) broadens the transition making resistive determination difcult. From this point of view, assertions of Kim et al.[Kim et al. [2006]] that their data allow one to distinguish between two models, GL and two-band Usadel approach by Gurevich,[Kamihara et al. [2008]] are hard to accept. In compounds with relatively high T_c , the determination of H_{c2} from resistive measurements is also complicated by the phenomenon of vortex lattice melting: above the melting point, the resistivity is close to that of the normal phase and H_{c2} per se becomes invisible in resistivity measurements. This complication in a given material might affect the measurements stronger near T_c than at low temperatures.

As can be seen from Figs. 4.2 the upper critical fields in H$||ab$ configuration are higher than the weak-limit paramagnetic limiting H_p , equal to 32.2 T (x = 0.054) and 13.8 T (x = 0.072). These high values may come from the strong coupling nature of superconductivity in iron pnictides, or indeed reflect paramagnetic limiting at low temperatures, as was suggested in several studies[Cho et al. [2011],Yuan et al. [2009],Terashima et al. [2009]].
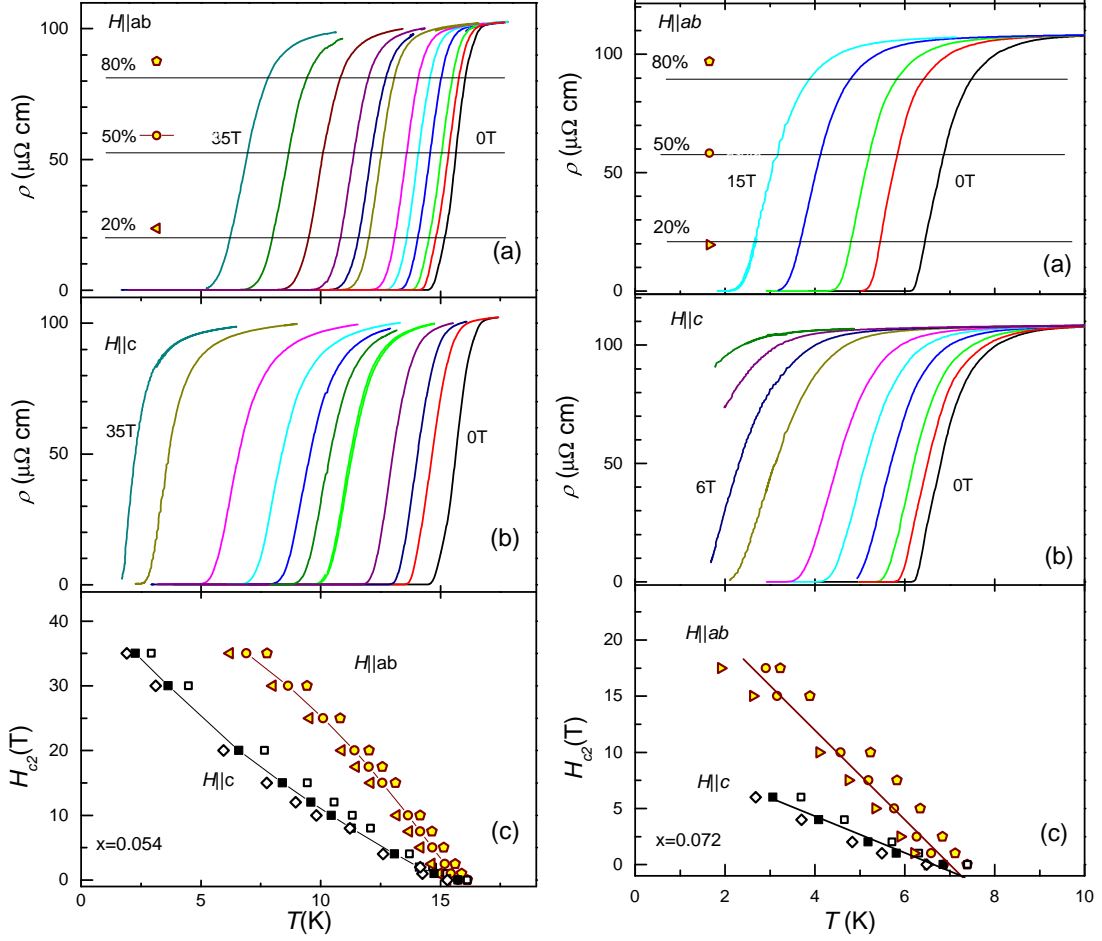
Figure 4.2 Right: In-plane resistivity ρ_a vs. temperature for slightly overdoped Ba(Fe$_{1-x}$Ni$_x$)$_2$As$_2$, x=0.054 in magnetic fields (a) parallel to the conducting ab plane; (b) parallel to the c-axis. Lines indicate 20, 50, and 80 % of the resistivity value immediately above the superconducting transition. Bottom panel (c) shows $H_{c2}(T)$ phase diagrams for both directions of magnetic field. Left: In-plane resistivity ρ_a vs. temperature for heavily overdoped Ba(Fe$_{1-x}$Ni$_x$)$_2$As$_2$, x=0.072 in magnetic fields (a) parallel to the conducting ab plane; (b) parallel to the c-axis. Lines indicate 20, 50, and 80 % of the resistivity value immediately above the superconducting transition. Bottom panel (c) shows $H_{c2}(T)$ phase diagrams for both directions of magnetic field.
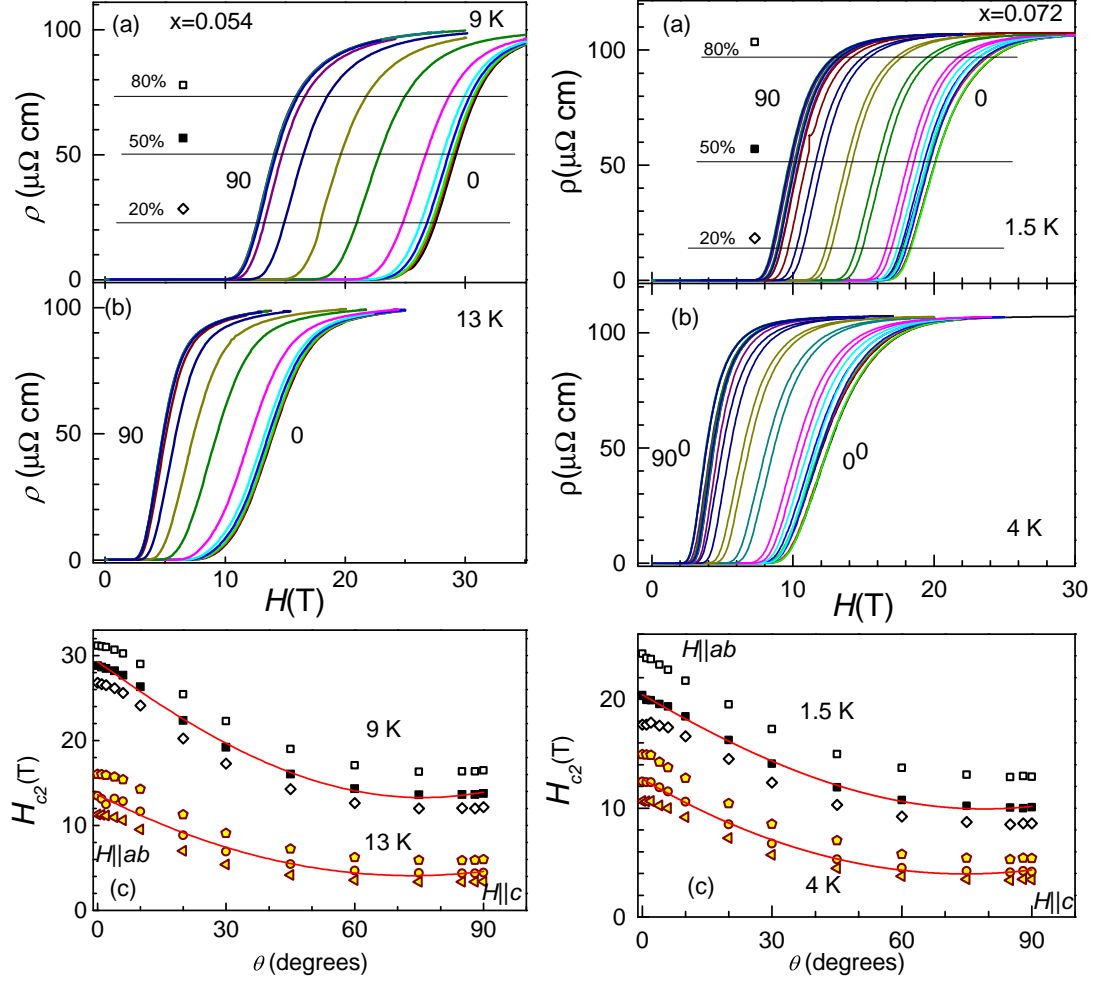
Figure 4.3 Right: Field dependence of in-plane resistivity $\rho(H)$ of slightly overdoped Ba(Fe$_{1-x}$Ni$_x$)$_2$As$_2$, x=0.054 sample at T=13 K (panel (a)) and T=9 K (panel (b)) with magnetic field inclination angle θ as a parameter. (c) Isotherms $H_{c2}(\theta)$, obtained at 9 K and 13 K, using 80%, 50% and 20% criteria. Solid line shows fit to Eq. 4.1. Left: Field dependence of in-plane resistivity $\rho(H)$ of strongly overdoped Ba(Fe$_{1-x}$Ni$_x$)$_2$As$_2$, x=0.072 sample at T=1.5 K (panel (a)) and T=4 K (panel (b)) with magnetic field inclination angle θ as a parameter. (c) Isotherms $H_{c2}(\theta)$, obtained 1.5 K and 4 K, using 80%, 50% and 20% criteria. Solid line shows fit to Eq. 4.1.
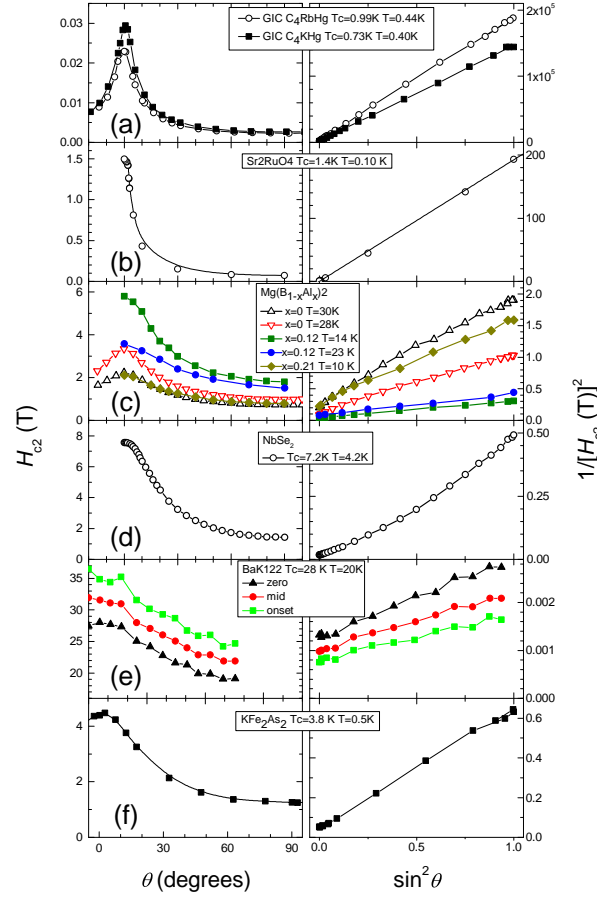
Figure 4.4 Analysis of the isothermal angular dependence of H_{c2} on inclination angle to the highly conducting plane θ, using linearization plot $H_{c2}^{-2}(\sin^2\theta)$. Left panels show digitized $H_{c2}(\theta)$, right panels plot the same data as $H_{c2}^{-2}(\sin^2\theta)$: (a) Graphite intercalation compounds [Iye and Tanuma [1982]] C_4RbHg (T_c=0.99 K, measurements taken at T_h=0.44 K, open circles) and C_4KHg (T_c=0.73 K, T_h=0.40 K, solid squares); (b) Sr_2RuO_4 (T_c=1.43 K, T_h=0.10 K,[Deguchi et al. [2002]]); (c) $Mg(B_{1-x}Al_x)_2$, [Kim et al. [2006]], x=0.12 (T_c=30.8 K, T_h=14 K, black solid squares, and T_h=23 K, red solid circles) and x=0.21 (T_c=25.5 K, T_h=10 K, blue open circles); (d) $NbSe_2$,[Morris et al. [1972]], (T_c= 7.2 K, T_h=4.2 K); (e) $(Ba_{1-x}K_x)Fe_2As_2$, [Yuan et al. [2009]], (T_c=28 K, T_h=20 K, using different criteria for resistive transition, zero resistance- black triangles, midpoint- red circles, onset - green squares); (f) KFe_2As_2, [Terashima et al. [2009]], (T_c=3.8 K, T_h=0.5 K).

Figure 4.5 Left: Angular dependence $H_{c2}(\theta)$, determined from fixed temperature $\rho(H)$ of Fig. 4.3 using 20%, 50% and 80% criteria (top to bottom), for slightly overdoped Ba(Fe$_{1-x}$Ni$_x$)$_2$As$_2$, x=0.054 at 9 K (top panel) and 13 K (bottom panel). The data are plotted as $H_{c2}^{-2}(\sin^2\theta)$, which according to Eq. 4.1 should be a straight line. Right: Angular dependence $H_{c2}(\theta)$, determined from fixed temperature $\rho(H)$ of Fig. 4.3 using 20%, 50% and 80% criteria (top to bottom), for strongly overdoped Ba(Fe$_{1-x}$Ni$_x$)$_2$As$_2$, x=0.0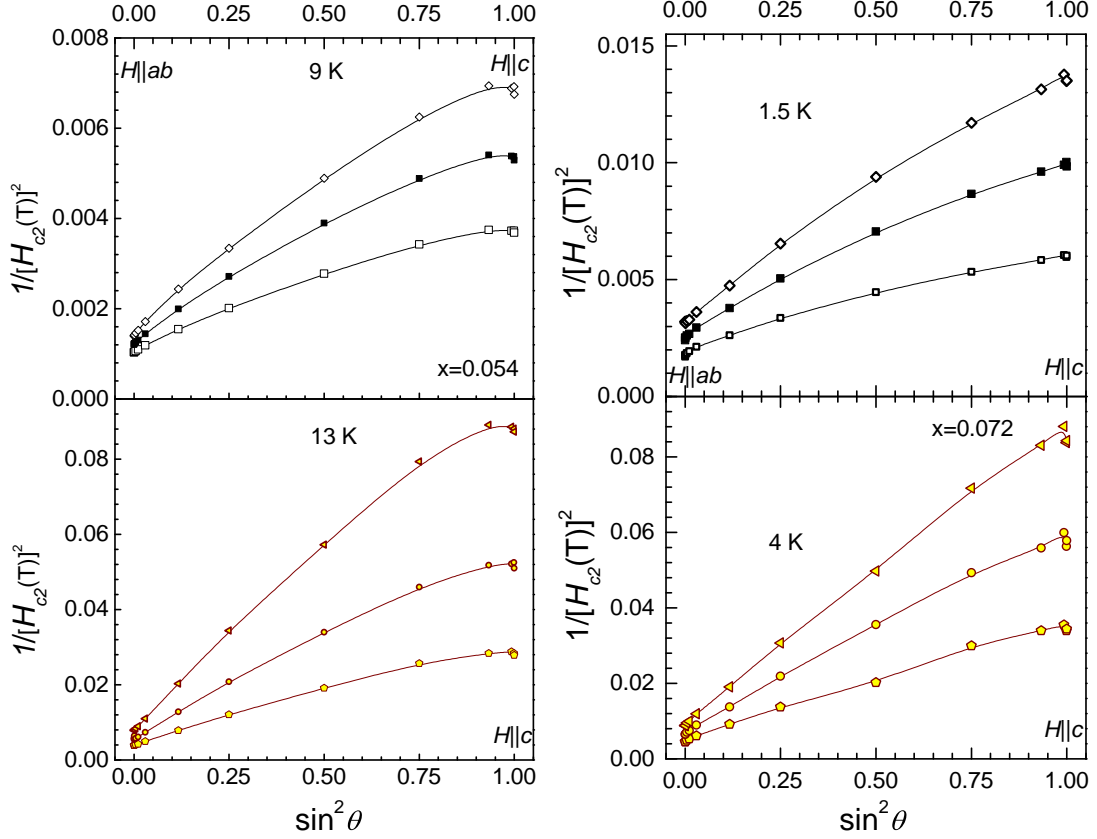72 at 1.5 K (top panel) and 4 K (bottom panel). The data are plotted as $H_{c2}^{-2}(\sin^2\theta)$, which according to Eq. 4.1 should be a straight line.

CHAPTER 5. Conclusion

5.1 Penetration depth of heavy-ion irradiated $Ba(Fe_{1-x}Co_x)_2As_2$

The temperature-dependent London penetration depth in overdoped samples of BaCo122, are best fit with power-law dependence $\Delta\lambda = AT^n$. The exponent n decreases with x towards the overdoped edge of the superconducting dome, consistent with development of gap anisotropy at the dome edge. The power law exponent n decreases from $n \approx 2.7$ in the x=0.108 down to $n \approx 2.0$ in the x=0.127. Heavy-ion irradiation decreases the exponent of the power law dependence in both x=0.108 from $n \approx 2.7$ down to $n \approx 2.2$, and in x=0.127 from $n \approx 2$ down to $n \approx 1.8$. Both this decrease of exponent and the value $n=1.8$, less than expected in s-wave accidental-node scenario, strongly supports a $s\pm$ pairing state universally over the whole doping range in electron-doped BaCo122.

5.2 Penetration depth of $SrFe_2(As_{1-x}P_x)_2$

Measurements of the London penetration depth, $\lambda(T)$, in optimally-doped as-grown and annealed single crystals of $SrFe_2(As_{1-x}P_x)_2$ iron-based superconductor provide clear evidence for line nodes. The absolute value of London penetration depth decreases with annealing from $\lambda(0) = 300\pm10$ nm to $\lambda(0) = 275\pm10$ nm. The slope $d\lambda/dt$=0.28 is consistent with the expectations for the superconducting gap with line nodes, $d\lambda/dt=\ln2/2.14=0.32$ which is comparable to the measured values in YBCO and BSCCO 2212.

Analysis of the temperature-dependent superfluid density, calculated using measured values

of the London penetration depth at T=0 regime , that the superfluid density $\rho(T)$ differs from the prediction for the vertical line nodes (as in a simple single - band $d-$wave) and requires an analysis within a full three - dimensional band-structure. Overall, our results indicate that $SrFe_2(As_{1-x}P_x)_2$ behaves very similarly to $BaFe_2(As_{1-x}P_x)_2$ both from transport and super-fluid response points of view and it seems that isovalently substituted pnictides are inherently different from the charge - doped materials.

5.3 Angular-dependent upper critical field of $Ba(Fe_{1-x}Ni_x)_2As_2$

By performing high angular resolution study of the upper critical field in two overdoped compositions of iron pnictide superconductor $BaFe_{1-x}Ni_xAs_2$, we find clear deviations from the anisotropic Ginzburg-Landau form. Implementing linearization plot analysis of our and previously published data, we find clear deviations from the form only in the case of multi-band superconductivity in pure $NbSe_2$ and MgB_2, but not in dirty MgB_2. We speculate, that the dependence may reflect c-axis modulation of the superconducting gap, as suggested by anisotropic penetration depth and thermal conductivity measurements [Tanatar et al. [2010c], Reid et al. [2010], Martin et al. [2010]].

Bibliography

Abrikosov, A. (1957). *Journal of Physics and Chemistry of Solids*, 2(3):199 – 208.

Abrikosov, A. A. and Gor'kov, L. P. (1960). *Zh. Eksp. Teor. Fiz.*, 39:1781.

Altarawneh, M. M., Collar, K., Mielke, C. H., Ni, N., Bud'ko, S. L., and Canfield, P. C. (2008). *Phys. Rev. B*, 78:220505.

Anderson, P. W. (1959). *J. Phys. Chem. Solids*, 11:26.

Bang, Y. (2009). *EPL (Europhysics Letters)*, 86(4):47001.

Bud'ko, S. L., Ni, N., and Canfield, P. C. (2009). *Phys. Rev. B*, 79:220516.

Canfield, P. C. and Bud'ko, S. L. (2010). *Annual Review in Condensed matter physics*, 1:27.

Carrington, A. (2011). *Reports on Progress in Physics*, 74:124507.

Cho, K., Kim, H., Tanatar, M. A., Song, Y. J., Kwon, Y. S., Coniglio, W. A., Agosta, C. C., Gurevich, A., and Prozorov, R. (2011). *Phys. Rev. B*, 83:060502.

Cho, K., Tanatar, M. A., Spyrison, N., Kim, H., Song, Y., Dai, P., Zhang, C. L., and Prozorov, R. (2012). *Phys. Rev. B*, 86:020508.

Deguchi, K., Tanatar, M. A., Mao, Z., Ishiguro, T., and Maeno, Y. (2002). *Journal of the Physical Society of Japan*, 71(12):2839–2842.

Doiron-Leyraud, N., Auban-Senzier, P., René de Cotret, S., Bourbonnais, C., Jérome, D., Bechgaard, K., and Taillefer, L. (2009). *Phys. Rev. B*, 80:214531.

Fletcher, J. D., Serafin, A., Malone, L., Analytis, J. G., Chu, J.-H., Erickson, A. S., Fisher, I. R., and Carrington, A. (2009). *Phys. Rev. Lett.*, 102:147001.

Gordon, R. (2011).

Gordon, R. T., Kim, H., Salovich, N., Giannetta, R. W., Fernandes, R. M., Kogan, V. G., Prozorov, T., Budko, S. L., Canfield, P. C., Tanatar, M. A., and Prozorov, R. (2010). *Phys. Rev. B*, 82:054507.

Gordon, R. T., Martin, C., Kim, H., Ni, N., Tanatar, M. A., Schmalian, J., Mazin, I. I., Bud'ko, S. L., Canfield, P. C., and Prozorov, R. (2009a). *Phys. Rev. B*, 79:100506.

Gordon, R. T., Ni, N., Martin, C., M. A. Tanatar, a. M. D. V., Kim, H., Samolyuk, G. D., Schmalian, J., Nandi, S., Kreyssig, A., Goldman, A. I., Yan, J. Q., Budko, S. L., Canfield, P. C., and Prozorov, R. (2009b). *Phys. Rev. Lett.*, 102:127004.

Gor'kov, L. (1987). *Sov. Sci. Rev. A Phys.*, 9:1.

Graser, S., Kemper, A. F., Maier, T., Cheng, H.-P., Hirschfeld, P., and Scalapino, D. (2010). *Phys. Rev. B*, 81:214503.

Hashimoto, K., Cho, K., Shibauchi, T., Kasahara, S., Mizukami, Y., Katsumata, R., Tsuruhara, Y., Terashima, T., Ikeda, H., Tanatar, M. A., Kitano, H., Salovich, N., Giannetta, R. W., Walmsley, P., Carrington, A., Prozorov, R., and Matsuda, Y. (2012). *Science*, 336:1554.

Helfand, E. and Werthamer, N. R. (1966). *Phys. Rev.*, 147:288–294.

Hirschfeld, P. J. and Goldenfeld, N. (1993). *Phys. Rev. B*, 48:4219.

Hirschfeld, P. J., Korshunov, M. M., and Mazin, I. I. (2011). *Reports on Progress in Physics*, 74(12):124508.

Iye, Y. and Tanuma, S.-i. (1982). *Phys. Rev. B*, 25:4583–4592.

J. Bardeen, L. N. Cooper, J. R. S. (1957). *Rev. Mod. Phys.*, 77:721.

Jacobs, T., Sridhar, S., Li, Q., Gu, G., and Koshizuka, N. (1995). *Phys. Rev. Lett.*, 75:4516.

Johnston, D. C. (2010). *Advances in Physics*, 59:803.

Kamihara, Y., Watanabe, T., Hirano, M., and Hosono, H. (2008). *Journal of the American Chemical Society*, 130(11):3296–3297.

Kim, H., Gordon, R. T., Tanatar, M. A., Hua, J., Welp, U., Kwok, W. K., Ni, N., Bud'ko, S. L., Canfield, P. C., Vorontsov, A. B., and Prozorov, R. (2010). *Phys. Rev. B*, 82:060518.

Kim, H.-J., Lee, H.-S., Kang, B., Yim, W.-H., Jo, Y., Jung, M.-H., and Lee, S.-I. (2006). *Phys. Rev. B*, 73:064520.

Lebed, A. and Sepper, O. (2012). *JETP Letters*, 96:176.

Liu, Y., Tanatar, M. A., Kogan, V. G., Kim, H., Lograsso, T. A., and Prozorov, R. (2013). *Phys. Rev. B*, 87:134513.

London, F. (1950). *Superluids Vol. I*.

Luan, L., Auslander, O. M., Lippman, T. M., Hicks, C. W., Kalisky, B., Chu, J., Analytis, J. G., Fisher, I. R., Kirtley, J. R., and Moler, K. A. (2010). *Phys. Rev. B*, 81:100501(R).

Mackenzie, A., Julian, S., Lonzarich, G., Carringon, A., Huges, S., Liu, R., and Sinclair, D. (1993). *Phys. Rev. Lett.*, 71:114502.

Maiti, S. and Chubukov, A. (2010). *Phys. Rev. B*, 82:214515.

Malone, L., Fletcher, J. D., Serafin, A., Carrington, A., Zhigadlo, N. D., Bukowski, Z., Katrych, S., and Karpinski, J. (2009). *Phys. Rev. B*, 79:140501.

Martin, C., Kim, H., Gordon, R. T., Ni, N., Kogan, V. G., Bud'ko, S. L., Canfield, P. C., Tanatar, M. A., and Prozorov, R. (2010). *Phys. Rev. B*, 81:060505.

Mazin, I. I. (2010). *Nature*, 464:183.

Müller, K. and Bednorz, J. G. (1987). *Advances in Physics*, 237:1133–1139.

Morris, R. C., Coleman, R. V., and Bhandari, R. (1972). *Phys. Rev. B*, 5:895–901.

Murphy, J., P., C., Strehlow, Cho, K., Tanatar, M. A., Salovich, N., Giannetta, R. W., Kobayashi, T., Miyasaka, S., Tajima, S., and Prozorov, R. (2013). *Phys. Rev. B*, 87:140505.

N. W. Ashcroft, a. N. D. M. (1976). *Solid State Physics*.

Nakai, Y., Iye, T., Kitagawa, S., Ishida, K., Ikeda, H., Kasahara, S., Shishido, H., Shibauchi, T., Matsuda, Y., and Terashima, T. (2010). *Phys. Rev. Lett.*, 105:107003.

Nakajima, M., i. Uchida, S., Kibou, K., Lee, C. H., Iyo, A., and Eisaki, H. (2012). *J. Phys. Soc. Jpn.*, 81:104710.

NakaJima, M., Ishiba, S., Kihou, K., Tomioka, Y., Ito, T., Yoshiba, Y., Lee, C. H., Kito, K., Iyo, A., Eisaki, H., Kojima, K. M., Kojima, K. M., and Uchida, S. (2010). *Phys. Rev. B*, 81:104528.

Ni, N., Thaler, A., Yan, J. Q., Kracher, A., Colombier, E., Bud'ko, S. L., Canfield, P. C., and Hannahs, S. T. (2010). *Phys. Rev. B*, 82:024519.

Ni, N., Tillman, M. E., Yan, J.-Q., Kracher, A., Hannahs, S. T., Bud'ko, S. L., and Canfield, P. C. (2008). *Phys. Rev. B*, 78:214515.

Norman, M. R. (2011). *Science*, 332(6026):196–200.

Paglione, J. and Greene, R. L. (2010). *Nature physics*, 6:645.

Poole, C. P., Farach, H. A., Creswick, R. J., and Prozorov, R. (2007). *Superconductivity*. Elsevier.

Posazhennikova, A. I., Dahm, T., and Maki, K. (2002). *EPL (Europhysics Letters)*, 60(1):134.

Prozorov, R., Giannetta, R., Carrington, A., and Araujo-Moreira, F. (2000a). *Phys. Rev. B*, 62:115.

Prozorov, R., Giannetta, R. W., Carrington, A. Fournier, P. G. R. L. G. P. H. D. G., and Banks, A. R. (2000b). *Applied Physics Letters*, 77:4202.

Reid, J.-P., Juneau-Fecteau, A., Gordon, R. T., de Cotret, S. R., Doiron-Leyraud, N., Luo, X. G., Shakeripour, H., Chang, J., Tanatar, M. A., Kim, H., Prozorov, R., Saito, T., Fukazawa, H., Kohori, Y., Kihou, K., Lee, C. H., Iyo, A., Eisaki, H., Shen, B., Wen, H.-H., and Taillefer, L. (2012a). *Superconductor Science and Technology*, 25(8):084013.

Reid, J.-P., Tanatar, M. A., Juneau-Fecteau, A., Gordon, R. T., de Cotret, S. R., Doiron-Leyraud, N., Saito, T., Fukazawa, H., Kohori, Y., Kihou, K., Lee, C. H., Iyo, A., Eisaki, H., Prozorov, R., and Taillefer, L. (2012b). *Phys. Rev. Lett.*, 109:087001.

Reid, J.-P., Tanatar, M. A., Luo, X. G., Shakeripour, H., Doiron-Leyraud, N., Ni, N., Bud'ko, S. L., Canfield, P. C., Prozorov, R., and Taillefer, L. (2010). *Phys. Rev. B*, 82:064501.

See, T. I. (2000). *J. Phys*, 139.

Shimojima, T., Sakaguchi, F., Ishizaka, K., Ishida, Y., Malaeb, W., Yoshida, T., Ideta, S., Fujimori, A., Kiss, T., Okawa, M., Togashi, T., Chen, C.-T., Watanabe, S., Nakashima, Y., Ino, A., Anzai, H., Arita, M., Shimada, K., Namatame, H., Taniguchi, M., S. Kasahara, T. T., Shibauchi, T., Matsuda, Y., Nakjima, M., Uchida, S., Kihou, K., Lee, C., Iyo, A., H. Eisaki, A. C., and Shin., S. (2012). *Solid State Commun.*, 152:695.

Suzuki, K., Usui, H., and Kuroki, K. (2011). *J. Phys. Soc. Jpn.*, 80:013710.

T. Kobayashi, S. Miyasaka, S. T. (2012). *J. Phys.: Condens. Matter*, 81SB:SB045.

Taillefer, L. (2010). *Annual Review in Condensed matter physics*, 1:51–70.

Tanatar, M. A., Hasimoto, K., Kasahara, S., Shibauchi, T., Matsuda, Y., and prozorov, R. (2013). *Phys. Rev. B*, 87:104506.

Tanatar, M. A., Ni, N., Bud'ko, S. L., Canfield, P. C., and Prozorov, R. (2010a). *Superconductor Science and Technology*, 23:054002.

Tanatar, M. A., Ni, N., Martin, C., Gordon, R. T., Kim, H., Kogan, V. G., Samolyuk, G. D., Bud'ko, S. L., Canfield, P. C., and Prozorov, R. (2009). *Phys. Rev. B*, 79:094507.

Tanatar, M. A., Ni, N., Thaler, A., Bud'ko, S. L., Canfield, P. C., and Prozorov, R. (2010b). *Phys. Rev. B*, 82:134528.

Tanatar, M. A., Reid, J.-P., Shakeripour, H., Luo, X. G., Doiron-Leyraud, N., Ni, N., Bud'ko, S. L., Canfield, P. C., Prozorov, R., and Taillefer, L. (2010c). *Phys. Rev. Lett.*, 104:067002.

Terashima, T., Kimata, M., Satsukawa, H., Harada, A., Hazama, K., Uji, S., Harima, H., Chen, G.-F., Luo, J.-L., and Wang, N.-L. (2009). *Journal of the Physical Society of Japan*, 78(6):063702.

Tinkham, M. (1996). *Introduction to superconductivity*. McGraw Hill, New York.

Tsuei, C. C. and Kirtley, J. R. (2000). *Rev. Mod. Phys.*, 72:969–1016.

V.G. Kogan, R. P. (2012). *Reports on Progress in Physics*, 75.

Vorontsov, A. B., Vavilov, M. G., and Chubukov, A. V. (2009). *Phys. Rev. B*, 79:140507.

Williams, T. J., Sczel, A. A., Baggio-Saitovitch, E., Bud'ko, S. L., Canfield, P. C., Carlo, J. P., Goko, T., Kageyama, H., Kitada, A., Munevar, J., Ni, N., Saha, S. R., Kirschembaun, K., Paglione, J., Sanchez-Candela, D. R., Uemura, Y. J., and Luke, G. M. (2010). *Phys. Rev. B*, 82:094512.

Xu, D., Yip, S., and Sauls, J. (1995). *Phys. Rev. B*, 51:16233.

Yuan, H. Q., Singleton, J., Balakirev, F., Baily, S., Chen, G., Luo, J., and Wang, N. (2009). *Letters to Nature*, 457:565–568.

Zhang, K., Bonn, D., Kamal, S., R. Liang, a. D. B., Handy, W., Basov, D., and Timusk, T. (1994). *Phys. Rev. Lett.*, 73:2484.

Zhu, Y., Cai, Z. X., Budhani, R. C., Suenaga, M., and Welch, D. O. (1993). *Phys. Rev. B*, 48:6436–6450.